Elevated temperature fatally disrupts nuclear divisions in the early *Drosophila* embryo.

Girish Kale[1,2,*], Pratika Agarwal[1], J Jaime Diaz-Larrosa[1], Steffen Lemke[1,2,*]

[1] Centre for Organismal Studies, University of Heidelberg, Heidelberg. Germany
[2] Institute of Biology, University of Hohenheim, Stuttgart, Germany
* Correspondance: G.K. (girish.kale@uni-hohenheim.de), S.L. (steffen.lemke@uni-hohenheim.de)

Abstract:

Temperature variations can challenge animal survival, with different life cycle stages presenting distinct vulnerabilities to elevated temperature. Here, embryonic development is known to be especially vulnerable to elevated temperature, though the molecular mechanism remain unclear. In this context, we investigate how elevated temperature affects embryogenesis in *Drosophila melanogaster*, utilizing it as a model with a well-characterized genetic makeup and developmental processes.

In *Drosophila* embryos, we identified the first three hours as a critical, temperature-sensitive time window. This period includes the formation of a syncytial blastoderm, which involves 4 rounds of meta-synchronous nuclear divisions at the embryo cortex, and cellularization that leads to formation of the cellular blastoderm. Embryos exposed to elevated temperature during this period showed increased lethality due to subsequent developmental defects during the gastrulation stage. We observed an increase in mitotic failures causing a loss of cortical nuclei, both, during syncytial blastoderm and cellularization stages in embryos developing at elevated temperature. Additionally, these embryos show a local crowding of nuclei and an increase in asynchrony between the nuclear cycles in the center vs. the poles. Interestingly, nuclear crowding and nuclear cycle asynchrony cooperatively amplify the frequency of mitotic failures, leading to holes in the blastoderm epithelium. We functionally tested known regulators of mitosis, to rescue these developmental defects and improve embryo survival, and asked whether existing wild populations carry signatures of adaptation in these regulators of mitosis.

Our genetic rescue experiments expose a vulnerability at elevated temperatures in the interaction between cortical F-actin and microtubules, leading to mitotic failures, which can be potentially rescued by modulating the expression of just a few factors. We propose that the expression levels of the corresponding genes could be used as indicators to predict fitness effects on insect populations that are exposed to increasing temperature variations.

Keywords:

Blastoderm formation, elevated temperature, microtubule - F-actin interaction, nuclear division defects, embryo lethality, genetic rescue, *Drosophila*

Introduction:

The current rise in global average temperatures and the amplitude of temperature fluctuations have been suggested to affect species fitness and result in a loss of biodiversity[1]. Though, it is not clear whether the effects on species fitness is direct consequnces of the temperature rise, in particular since for many species it presumably still represents a rather gradual departure from previously evolved, species-specific temperature optima. Previous studies suggest that such gradal departure could, under certain circumstances, impact animal suvival. For instance, studies have shown the occurrence of birth defects due to high fever during pregnancy in humans[2–4], indicating that the same temperature condition is more detrimental to the embryo than it is to the adult. This raises the possibility that specific characteristics of embryo development renders it more vulnerable to temperature increase. Consistent with this interpretation, previous studies in model organisms have shown that temperature is a key factor that determines the fidelity of embryonic development, with rat and zebrafish embryos showing an increase in developmental defects at elevated temperatures[5–8]. Despite these findings, it is unclear what leads to vulnerability in embryonic development at elevated temperatures. In this context, we explore whether the exposure to elevated temperature is detrimental to embryonic development in *Drosophila melanogaster* (henceforth, *Drosophila*), asking what are the consequences in terms of population-level parameters, such as embryo survival.

In nature, animals rarely experience steady temperatures and show adaptation to a certain range of temperatures that they would naturally experience. Studies have reported acceleration in a variety of physiological processes with increasing temperature, including development, growth, and regeneration[9]. Thus, in this range, time appears to be a function of temperature. Here, the Arrhenius equation, which describes the effect of temperature on the rates of biochemical reactions, also adequately describes the effect of temperature on the rate of physiological processes, especially embryonic development[10,11]. However, in contrast to chemical reactions, physiological processes observe this relationship within a rather narrow range of temperatures. In *Drosophila*, the transition from 28°C to 30°C no longer shows an acceleration of embryonic develoment[10–12], suggesting that 29°C represents a first possible threshold at which the development is challenged at elevated temperature. Thus, we tested developmental fidelity at this elevated temperature of 29°C, as compared to controls at the normal culture temperature of 25°C.

Previous studies have found that *Drosophila* embryo development beyond the first 4-6 hours is robust to even acute exposure to high temperatures[13], suggesting that the potential embryonic vulnerabilities in *Drosophila* could be uncovered in these first few hours of development. The first few hours of development in *Drosophila* starts with fertilization. After fertilization, the embryos undergo 9 rounds of syncytial nuclear divisions deep in the yolk. Following these divisions in the yolk, most nuclei migrate to the embryo periphery, where 4 more rounds of nuclear division take place during a stage called syncytial blastoderm[14]. In the syncytial blastoderm, nuclear divisions are facilitated by pseudo-cleavage furrows, i.e., temporary membrane invaginations resembling a half-cell that slowly form around the nuclei during interphase-metaphase, and are then rapidly reabsorbed into the embryo cortex during anaphase-telophase[15]. Following a total of 13 nuclear divisions, the resulting ~6000 nuclei simultaneously segregate into individual cells and produce the blastoderm epithelium in a process called cellularization [16]. At this point, about 3 hrs from fertilization, gastrulation starts, which involves cell shape changes[17], cell contact rearrangements[18], and further rounds of cell divisions in isolated mitotic domains[19]: all facilitating the early morphogenesis.

In our experiments, we found that exposing embryos to 29°C during the first 3 hours of embryonic development leads to a significant increase in population-level embryonic lethality, where embryo lethality occurs during the gastrulation stage. Detailed examination revealed mitotic failures leading to the loss of

nuclei during the syncytial blastoderm and cellularization stages. Additionally, embryos developing at 29°C showed nuclear crowding in the central region of the embryo, as well as greater asynchrony in the nuclear division cycles between central regions vs. anterior/posterior poles of the embryo. Moreover, we could show that the nuclear crowding and nuclear cycle asynchrony combinatorially increase the local propensity of mitotic failures. Such local increase in mitotic failures results in holes in the blastoderm, i.e., a region devoid of nuclei/cells, which disrupts the continuity of this primary epithelial tissue. To rescue these defects, we experimented with overexpressing certain genes that regulate cell polarity, microtubule-F-actin interactions, and mitotic spindle orientation, aiming to enhance the resilience of nuclear divisions at 29°C. Our results suggest a vulnerability in microtubule- F-actin interaction during the well-conserved process of nuclear division at elevated temperatures. Our analysis of the data on genetic variation in natural populations revealed an overlap with candidate genes in our experiments. Taken together, our work not only identifies cell biological defects caused by elevated temperatures but also links them to population-level lethality and fitness, offering insights into the broader implications of vulnerability to elevated temperatures during embryonic development.

Results:

Early exposure to elevated temperature reduces embryo survival due to gastrulation defects

To explore how elevated temperature affects the early development of *Drosophila* embryos, we exposed young embryos to 29°C and asked how many of them survived and how they developed. To investigate alterations in the rate of embryos hatching into larvae, we first differentiated the effects of temperature exposure by timing: from the moment of deposition until just before gastrulation begins (~3 hours), and during a similar time starting from gastrulation onset (refer to Figure 1A for experimental temperature regimen). In both scenarios, we observed a notable increase in embryonic lethality (Figure 1B), pinpointing a critical vulnerability especially during the pre-gastrulation phase of development. This finding was unexpected, as prior research suggested that the genetic mechanisms governing embryonic patterning during this phase were resilient to temperature fluctuation[20,21], indicating a more systemic effect, possibly rooted in cell biology.

To address when and how embryos died after early exposure to 29°C, we maintained embryos until the late cellularization stage at 29°C and then continued to observe their development using confocal microscopy time-lapse recordings at 25°C. Embryonic development in these recordings was analyzed qualitatively as well as quantitatively. Qualitatively, many embryos displayed moderate anomalies during gastrulation, including twisting along the embryo's anterior-posterior axis (Figure 1C-D), exemplifying the defects in the bilateral symmetry of embryonic development. Notably, these twisted embryos seemed to recover from their defects and continued to develop. By contrast, a minority of embryos exhibited severe gastrulation defects, culminating in developmental cessation and lethality (Figure 1E). Quantitatively, surviving embryos after exposure to 29°C did not differ statistically significantly from those after control exposure to 25°C, neither in the rate of germband extension (GBE, Figure 1F) nor in the timing of other key developmental milestones (Figure 1G). Overall, this suggests that if embryos surpass the gastrulation stage, they proceed without detectable developmental delays.

Taken together, our findings underline increased embryonic lethality during gastrulation due to prior exposure to 29°C, highlighting the detrimental effects of our elevated temperature. While the lethality occurs during the gastrulation stage, the surviving embryos show defects in bilateral symmetry. Given that the genetic patterning is robust to temperature perturbations[20,21], we hypothesized that the nuclei, where this patterning information is interpreted, might exhibit defects in certain aspects of their dynamic

behavior. Thus, we decided to further investigate nuclear dynamics during these critical early developmental hours.

A clustered loss of nuclei at elevated temperature likely causes gastrulation defects and embryo lethality

Our finding that exposure to 29°C in the first three hours of development can result in increased gastrulation failures suggests that pre-gastrulation development in flies exhibits vulnerability to elevated temperatures. Pre-gastrulation development in flies and other insects involves nuclei dividing deep within the yolk before moving to the embryo's cortex, where they must be securely anchored while undergoing further rounds of division. Ultimately, the tight and even distribution of those syncytial nuclei at the egg cortex is crucial for the generation of blastoderm epithelium and its subsequent morphological changes during gastrulation.

To address whether defects during gastrulation could stem from defective blastoderm, we focused our analyses on the distribution of cortical nuclei during cellularization, i.e., just before gastrulation, using fixed embryos stained for DNA to visualize nuclei in the entire embryo volume. In embryos developing at 29°C, we observed a subcortical cluster of nuclei in a small fraction of embryos (Figure 2A), which corresponded to a hole in the cortical layer of nuclei. To better visualize and differentiate cortical and subcortical nuclei, we segmented the embryo volume and color-coded the image voxels based on their distance from the embryo surface (Figure 2B). We noticed a few subcortical nuclei in embryos developing at normal temperature (Figure 2C, F), while a large fraction of embryos developing at 29°C showed an increase in subcortical nuclei, albeit not in large clusters (Figure 2D, G). Notably, however, in a small fraction of embryos developing at 29°C, we observed a hole in the cortical layer of nuclei, coinciding with a subcortical cluster of at least 10 nuclei (Figure 2E, H). In the coordinate system of the embryo, the distribution of subcortical nuclei wasn't left-right symmetric either, and the location of the subcortical clusters of nuclei varied across embryos, albeit being localized in the central region of the embryo.

To investigate the underlying cause for subcortical nuclei, we followed nuclear dynamics using time-lapse recordings; Histone-RFP was used to visualize chromatin, and Jupiter-GFP to visualize microtubules for keeping track of nuclear division cycles. Starting with nuclear migration from the yolk to the periphery (occurring during the interphase of the 10th nuclear cycle), we observed nuclei through their peripheral divisions during syncytial blastoderm (through mitoses 10 to 13), then through cellularization (interphase 14), and until the onset of gastrulation could be inferred from the movement and division of nuclei (beyond interphase 14). The nuclear translocation during interphase 10, from deep inside the yolk to the embryo cortex, was comparable between embryos developing at 25°C and those at 29°C. However, during the syncytial blastoderm stage and cellularization, embryos that developed at 29°C much more frequently "lost" nuclei from their cortical layer than if they developed at 25°C, i.e., nuclei that were initially positioned within the cortical layer of the egg, appeared to get expelled, descended into the yolk, and did not become part of the embryonic blastoderm (Figure S1, also see below), with variability in the extent of the nuclear loss, producing holes in the blastoderm of a fraction of embryos (Figure S2).

Taken together, in pre-gastrulation embryonic development we narrowed down the developmental vulnerability at 29°C to the syncytial blastoderm stage and cellularization, where we see nuclear loss from the embryo cortex. Notably, the fraction of embryos showing clustered loss of nuclei during cellularization (Figure 2A) was similar to the fraction of embryos with gastrulation defects (Figure 1F) and was consistent with embryo lethality at 29°C (Figure 1B). The embryo-to-embryo variability, both in the distribution and intensity of nuclear loss, further argued for the possibility that these defects were not dictated by defective embryonic patterning. While consistent with the idea that nuclear loss was causing the observed increase in embryonic lethality, the temperature-dependent mechanism leading to nuclear loss was still unclear. To

further address the mechanistic link between elevated temperature and the dislodging of nuclei from the cell cortex, we decided to study the process in more quantitative detail.

At elevated temperature, embryos lose nuclei from the cortex after defective divisions.

A closer look at the loss of cortical nuclei indicated that the nuclei were lost either individually or as pairs of two adjacent nuclei. Thus, we decided to quantify these causes of nuclear loss to identify their contribution to the early developmental vulnerability to elevated temperatures.

We first focused on the isolated loss of nuclei. An isolated nucleus could be lost by a division perpendicular to the embryo surface (out-of-plane division), where the nucleus facing the inside of the embryo may not get properly anchored to the cortex and is consequently lost into the yolk. Alternatively, an isolated nucleus may be lost after an in-plane division, e.g. if steric hindrance and insufficient space would not allow for simultaneous anchoring of two adjacent nuclei to the embryo cortex. To account for these possibilities, we visually tracked all lost nuclei back in time to their last division.

Out-of-plane divisions could be detected in embryos at all of our experimental temperatures. These out-of-plane divisions could be easily identified, as they formed a characteristic mitotic spindle that was oriented perpendicular to the embryo surface (Figure 3A), and after the division only one of the daughter nuclei remained attached to the cortex. However, out-of-plane divisions occurred only during the mitoses of the 10th nuclear cycle, thus couldn't explain the loss of nuclei from the 11th nuclear cycle onwards. Loss of nuclei following an in-plane division could also be detected. These losses occured at a low frequency throughout the syncytial blastoderm stage and cellularization, at all of our experimental temperatures (Figure 3B). When we quantified the isolated loss of nuclei, we noted that the overall frequency of out-of-plane divisions was very low (<5%) (Figure 3C), and loss of individual nuclei after an in-plane division was rather infrequent, and albeit occurring more frequently during interphase 14 (cellularization), it did not differ significantly within the range of experimental temperatures (Figure 3D). The overall extremely low frequency of isolated nuclear loss – even in embryos developing at 29°C – strongly suggests that isolated nuclear loss was not the main driver of temperature-dependent nuclear loss in the fly blastoderm.

Next, we focused on the pairwise losses of nuclei. As above, we tracked lost pairs of nuclei to their last division cycle. This tracking revealed that every pairwise loss of nuclei was, in fact, a loss of sister nuclei. This observation suggested that specific characteristics of cortical nuclear divisions might determine the future fate of the newborn nuclei and trigger their release from the egg cortex, possibly in response to failed checkpoints. Consistent with this idea, we observed chromosome segregation defects preceding the pairwise loss of nuclei (Figure 3E), at all of our experimental temperatures. Because chromosome segregation defects can lead to aneuploidy, our observations suggested that the subsequent expulsion of daughter nuclei from the egg cortex was due to prior defective mitosis. To address whether the observed loss of nuclei at 29°C could be attributed to an overall increase in defective mitoses, we asked if their frequency was changing depending on the temperature (see methods). For this, we focused on interphase 14, which is when we observed the most nuclear losses. While the frequency of mitotic failures was overall low at 22 to 28°C, it increased significantly at 29°C (Figure 3F). Of note, defective mitoses at normal or elevated temperature were not associated with a stereotypical time course of nuclear expulsion. Defective nuclei could be lost in the interphase immediately following defective divisions, or later (Figure S3), suggesting that nuclear expulsion after defective mitosis was a passive process and not triggered by molecular signaling at failed checkpoints.

Taken together, our findings identify nuclear divisions in the blastoderm as a thermolabile cellular process that shows a disproportionate increase in failures with the transition from 28°C to 29°C, resulting in the loss

of sister nuclei from the egg cortex, when born in defective mitoses. However, which characteristics of nuclear divisions render them thermolabile was unclear.

At elevated temperature, nuclei displace drastically, especially during divisions.

For embeyos at 25°C, we noted that the nuclei were rather dynamic in their localization, showing local movements, throughout the syncytial blastoderm stage. For embryos at 29°C, this dynamicity increased, and we could see nuclei being displaced rather drastically. We hypothesized that such displacement poses a challenge to nuclear anchorage at elevated temperatures, especially during mitosis, causing mitotic defects and the paired loss of nuclei. To that end, we tracked nuclear clusters starting from individual mother nuclei at end of interphase 10 to the 8 great-granddaughter nuclei at end of interphase 13. At each time point, we computed the position of the nuclear cluster, using the center of the positions of the nuclei in that cluster, yielding one track per cluster (Figure S4A-C, also see methods). Our tracking showed that the nuclear clusters had two components to their movement, a global drift and a local displacement.

First, the clusters exhibited a global consistant drift-like movement, which represented a concerted global movement of all nuclei. We captured this component using a linear fit to the tracks of the center of the nuclear clusters over time (Figure S4B dotted lines). The slope of the linear fit indicated that the clusters drifted towards the posterior end at all of our experimental temperatures (Figure S4D, E). This component of nuclear movements was reminiscent of the previously reported dynamics reordering of nuclei in the early syncytial blastoderm[22]. Notably, however, the extent of nuclear cluster drift did not correlate with the occurance of blastoderm holes (Figure S4D, large hollow markers).

Second, independent of this drift, we observed local deviations in the position of the nuclear clusters over time. These local deviations were measured relative to the global drift. We reasoned these local deviations could be a proxy for mechanical stresses experienced by the nuclear division machinery during interphase-metaphase and anaphase-telophase. The deviations relative to the constant drift were more drastic along the anterior-posterior (AP) axis (Figure S4F, H) than those along the dorsal-ventral (DV) axis (Figure S4G, I), and deviations during the anaphase-telophase period (Figure S4H, I) were more drastic than those during the interphase-metaphase period (Figure S4F, G). In the context of length scales typical for nuclear divisions, this meant that cluster displacements in embryos developing at 25°C and during anaphase-telophase were comparable to that of the length of the spindle itself, while for embryos at 29°C, cluster displacements could be up to 4-fold higher. This increase in cluster displacements suggested increased mechanical stresses especially during the critical anaphase-telophase period, indicating an extensive propensity for displacement relative to embryo cortex at a time when the dividing nuclei need to be robustly anchored to the embryo cortex. Consistent with this interpretation, embryos with blastoderm holes showed greater nuclear cluster deviations especially during anaphase-telophase (Figure S4H, large hollow markers).

In addition to the analysis of nuclear movements parallel to the embryo cortex we wondered about the movements orthogonal to cortex, i.e., the future apical-basal (AB) axis in the blastoderm cells[23]. We again focused on the anaphase-telophase period, given the defects above. In embryos developing at 25°C, we observed that nuclei maintained a constant distance from the cortex (Figure S5A). However, in embryos developing at 29°C, we could see two waves of nuclear displacement towards the cortex, which originate from the anterior and the posterior, and meet at the central region of the embryo (Figure S5B). These waves of nuclear displacement were tightly correlated with waves of nuclear divisions, with peaks of the waves corresponding to anaphase-telophase transition. This suggests that as nuclei divide the spindle moves upwards, to gain more space. This need for space indicated additional challenages for the spindles during nuclear division, explaining, at least in parts, the mitotic failure at 29°C.

Taken together, our quantifications and observations captured an embryo-wide increase in nuclear displacement locally, along the AP- and AB-axis, and argued for the possibility of mechanical defects during nuclear divisions at 29°C, rendering them thermolabile. In a fraction of embryos, the mitotic failures occurred in great numbers and in close vicinity, leading to holes in the blastoderm epithelium at 29°C (Figure 3F, hollow markers), and these embryos also exhibited greater displacement of nuclei during anaphase-teophase (Figure S4H, hollow markers). However, our quantifications and observations of an increased nuclear displacement didn't establish a direct link with clustered nuclear loss. Thus, although the formation of blastoderm holes (Figure S2) could be directly attributed to clustered mitotic failures, it remained unclear why mitotic failures were stochastically distributed in most embryos, yet locally clustered in the central region of at least some embryos.

Nuclei divide with a time shift and are crowded in embryos at elevated temperature.

To better understand the differences between stochastic mitotic failures and locally clustered failures, we focused on cases with severe nuclear losses in embryos at 29°C. The most severe loss of nuclei in embryos at 29°C was often observed in the central domain of the embryo (Figure 2, Figure S1 and S2). Thus, we wondered if the central regions of the embryo were somehow special, and if there were characteristics in nuclear divisions or nuclear distribution that rendered the central regions to be distinct than the anterior/posterior poles.

As mentioned above, the central regions of the embryos at 29°C coincided with the "collision" of two waves of nuclear divisions (Figure S5). This observations was in stark contrast with embryos at 25°C, where nuclear divisions are meta-synchronous[24], with anterior-posterior waves (Figure 4A). We could further observe that, at 29°C, phases of nuclear division in the central region were lagging behind those at the anterior/posterior pole of the embryos. This resulted in neighboring regions of the embryo showing sequential phases of nuclear division at the same time (Figure 4B), in contrast to the meta-synchrony at 25°C. Conversely, the same phase of the nuclear division cycle could be observed at different time points in different regions of the embryo (Figure S6A-B). Thus, we decided to quantify this asynchrony of nuclear division cycles as a function of temperature (see methods). Our quantifications show that the asynchrony significantly increases in embryos developing at 29°C as compared to other temperatures (Figure 4C). This indicated that the central region of the embryo is distinct from the poles in nuclear division dynamics, with the phases of the nuclear cycle lagging.

The central region of the embryo, which corresponded to the delayed nuclear division cycles, also had more tightly packed nuclei. To quantify nuclear crowding, we focused on the end of interphase 13 (see methods), as that's the time we observed maximum nuclear crowding, before the most intense nuclear loss. To quantify the space available for cortical blastoderm nuclei, we segmented the nuclei and used Voronoi tessellation to define a region around each nucleus, which we call pseudo-cells. The areas of pseudo-cells were rather homogeneous in embryos developing at 22°C (Figure 5A, E, I). Already at 25°C (Figure 5B, F, J) and 28°C (Figure 2C, G, K), the available space for cortical nuclei was no longer uniform across the embryo, and it showed signs of local crowding in the central regions of the embryo. At 29°C, the space available for nuclei along the anterior-posterior axis varied substantially and revealed strong nuclear crowding in the central region of the embryo (Figure 5D, H, L). We quantified the extent of crowding (see methods) as a function of temperature, and found a progressive increase in nuclear crowding (Figure 5M). Thus, we also quantitatively describe the defect of nuclear crowding at 29°C, to demonstrate that the central region of the embryo is distinct from the poles in inter-nuclear spacing, with nuclei being more crowded in the central regions.

Taken together, in the central regions, nuclear division cycles lag behind those at the anterior/posterior poles, and nuclear density is greater than that at the anterior/posterior poles. It is conceivable that an asynchrony in nuclear cycles leads to mitotic failures due to a mismatch between the state of nuclear cycle in the central regions and the cell cycle signaling state of the syncytium. Additionally, local crowding of nuclei could conceivably produce mitotic failures by limiting the space available for mitotic spindles. Given that blastoderm holes also appear in the central regions of the embryo, we hypothesized that the clustering of mitotic failures (leading to blastoderm holes) at 29°C was dictated by either the regions of highest nuclear crowding, or the most delayed nuclear cycles, or both.

Region of embryo with greater nuclear crowding and with delayed nuclear cycles are associated with greater frequency of mitotic failures.

To test whether nuclear crowding and/or nuclear cycle asynchrony resulted in a predisposition towards a local increase in mitotic failure, we first defined the regions of the embryo with high nuclear crowding (Figure 6A), or regions with substantially delayed nuclear division cycles (Figure 6B). In parallel, we marked the locations of mitotic failures during cellularization, which could be overlaid on any predefined region to calculate the fraction of mitotic failures in that region. Then, to measure the fraction of mitotic failures associated with either nuclear crowding, or nuclear cycle asynchrony, or both, we constructed the regions of the embryo with; either the high nuclear crowding, i.e., crowded regions (Figure 6C); or substantial delay in nuclear division cycles, i.e., delayed regions (Figure 6D); or a combination of crowded and delayed regions, i.e., combined region (Figure 6E) (see methods).

In crowded regions, the fraction of mitotic failures increased progressively with higher temperatures, with statistical significanct differences between 22 and 29°C (Figure 6F). In delayed regions, the fraction of mitotic failures showed an abrupt increase from 28 to 29°C, albeit with only marginal statistical significance (Figure 6G). In the combined regions, the fraction of mitotic failures was greater than those in the crowded or delayed regions alone (Figure 6H). Additionally, the increase in the fraction of mitotic failures in any of these regions, as a function of temperature, could not be explained by the changes in area fractions themselves as a function of temperature (Figure S7). This suggests that temperature-dependent nuclear crowding and cycle asynchrony both contribute to a predisposition towards mitotic failure in the syncytial blastoderm, and that nuclear crowding has a stronger impact than nuclear cycle asynchrony.

Taken together, we show that the spatial distribution of overlap between nuclear crowding and nuclear cycle asynchrony is necessary to explain why clustered mitotic failures occur more frequently in the central region of the embryo, leading to blastoderm holes.

Identifying vulnerabilities in a deeply conserved cellular process at elevated temperature

The finding that mitosis in the early blastoderm constitute a temperature labile process, and that nuclear crowding and cycle asynchrony can at elevated temperatures can drive clusted nuclear loss, suggested vulnerabilities in core molecular interactions that control nuclear divisions in the early fly embryo. To address how a deeply conserved and presumably robust process like mitosis could be affected so dramatically due to a mere 4°C rise in temperature, we asked whether increasing expression levels of critical components in the nuclear division machinery could help to rescue the observed defects at 29°C. Cortical syncytial nuclear divisions in the fly embryo rely on transient metaphase furrows of the embryo cortex. These furrows are slowly formed through the insertion of membrane between nuclei during interphase, after which the mitotic spindles are formed parallel to the surface during pro- and metaphase, with a rapid regression of the furrows during ana- and telophase. As such, these furrows are reestablished during each nuclear cycle, and include reestablishment of cell polarity and reorganization of cytoskeletal

elements[23]. The dependence on transient membrane invaginations to establish cell polarity information is the most significant deviation from canonical cell divisions in eukaryotes and represents a evolutionary young and potentially labile element of cortical nuclear divisions in insect embryos. To test whether the fidelity of cortical mitoses at elevated temperatures hinges upon insufficiently robust cell polarity signaling, we sought to strengthen cell polarity signaling by increasing the abundance of two prominent polarity proteins that are known to be active in the syncytial blastoderm, Bazooka (baz, a Par-3 homolog) and Disks-large (dlg)[25]. Specifically, we asked whether overexpression of either protein had the capacity to bring lethality at 29°C back to normal, and if so, whether the increase in the fraction of mitotic failures in crowded and combined regions were rescued as well.

In embryos at 25°C, we did not observe a significant change in embryo lethality with increased levels of either baz or dlg as compared to control embryos with wildtype levels of baz and dlg (Figure S8A). At 29°C, lethality increased in control embryos with wildtype levels of baz and dlg (Figure S8A), similar to results in previous experiments (Figure 1B). By contrast, embryos with increased levels of either baz or dlg performed notably better at 29°C, with lethality reducing to about two-thirds (increased baz levels) and half (increased dlg levels) of the controls (Figure S8A). We note however that the rescue of lethality at 29°C in *baz* over-expressing embryos was only marginally significant, with a lot of variability between samples. Additionally, *dlg* over-expressing embryos at 25°C showed higher variability in embryo lethality than their control counterparts. Consistent with these results, *baz* over-expression did not rescue the increase in the fraction of mitotic failures, either in the crowded regions or in the combined regions at 29°C (Figure S8B, C), though the large blastoderm holes were absent in these embryos. Then, *dlg* over-expression rescued the increase in the fraction of mitotic failures only in the crowded region at 29°C (Figure S8B, C), and while the large blastoderm holes were absent in these embryos, *dlg* over-expression increased the fraction of mitotic defects at normal temperature in both, the crowded region and in the combined region, occasionally producing small blastoderm holes (Figure S8B, C). These results indicated that the establishment of polarity cues during syncytial divisions was robust, and suggested that temperature-dependent vulnerability was more specific to the subsequent cytoskeletal regulation that establishes the core mitotic spindle.

To establish and anchor a mitotic spindle to the cortex of the egg requires a dynamic interaction between microtubules and F-actin, which together anchor chromatin at the cortex throughout nuclear division[23]. So to faithfully pull sister chromatids towards the actin cortex on either side of the division plane, the execution of mitosis relies on tightly regulated interactions between the actin cortex and the microtubules of the mitotic spindle[26,27]. In *Drosophila*, these critical interactions of actin and microtubules have been associated with a complex of three proteins: α-Catenin (αCat), which binds to the cortical F-actin; β-Catenin (βCat, or armadillo in *Drosophila*), which binds to α-Catenin; and Adenomatous polyposis coli 2 (Apc2), which links to βCat and binds to the microtubules of the mitotic spindle[28]. Within this tripartite complex, the interaction of αCat and βCat is direct and is presumably not regulated, whereas the interaction of βCat and Apc2 is mediated by a specific kinase, the *Drosophila* homolog of the Glycogen Synthase Kinase 3β, Shaggy (sgg)[29].

We reasoned that, if this tripartite protein complex was thermolabile, then our high temperature conditions should, at least in parts, phenocopy the loss of function of one of the components of the complex (αCat, βCat, or Apc2) or sgg. The loss of function of this protein complex has been associated with an "empty actin caps" phenotype, where cortical dome-like structures of F-actin are no longer associated with nuclei[28]. Thus, to test for the possibility that this tripartite protein complex is thermolabile during early embryonic development in *Drosophila*, we analysed embryos that were fixed and stained to visualize nuclei and cortical F-actin (see methods). At control temperature of 25°C, we see a tight association between nuclei and F-actin during interphases in the syncytial blastoderm, where cortical F-actin surrounds each

383 nucleus, forming the actin cap. Notably, we can see the gaps between neighboring actin-caps in cases of
384 recently expelled nuclei (Figure S9C), or in cases where the spacing between nuclei is large enough (Figure
385 S9D). In contrast to controls at 25°C, in embryos that developed at 29°C we could observe the empty actin
386 caps phenotype (Figure S9F), reminiscent of that in embryos mutant for *Apc2* or β*Cat* (see Figure 3d-f in
387 McCartney et al. 2001[28]). Thus, we hypothesized that stabilizing the activity of the complex, through
388 elevated levels of αCat, βCat, Apc2, or sgg, could increase the fidelity of cortical mitoses at 29°C, through a
389 tighter control of actin and microtubule coupling to decrease the fraction of mitotic failures in crowded and
390 combined regions, ultimately attenuating embryonic lethality.

391 We decided to test the effects of elevated levels of either αCat or sgg on embryo lethality at the control
392 and elevated temperatures, using over-expression constructs for either gene, and quantified embryo
393 lethality. At 25°C, we did not observe a significant difference in embryo lethality between control embryos
394 and those with elevated levels of αCat or sgg (Figure 7A). At 29°C, lethality was overall increased in
395 controls, similar to results in other similar experiments (Figure 1B, Figure S7A). By contrast, embryos with
396 elevated levels of either αCat or sgg survived significantly better at 29°C, with lethality reducing to about
397 half (increased αCat levels) or a third (increased sgg levels) relative to the controls (Figure 7A). Consistent
398 with these results, large blastoderm holes were absent in these embryos, and the fraction of mitotic
399 failures in crowded as well as in the combined regions was reduced compared to control embryos at 29°C
400 (Figure 7B, C). These results indicate that the experimental strengthening of actin-binding is able to
401 attenuate temperature-dependent destabilizations of the mitotic spindle, suggesting that the scaffolding
402 activity of αCat, βCat, and Apc2, mediated by sgg, constitutes a thermosensitive controller of nuclear
403 division fidelity in the syncytial *Drosophila* embryo.

404 To test whether thermosensitivity of nuclear division fidelity was dependent specifically on the scaffolding
405 activity of αCat, βCat, and Apc2 rather than a common capacity of any regulator of mitotic spindle, we
406 asked whether the elevated levels of other regulators could similarly increase robustness against elevated
407 temperatures. To address this question, we focused on regulators known to dictate the orientation of the
408 mitotic spindle during cell division[30]. Both, the activity of 'Mushroom body defect' (mud, NuMA homolog)
409 and that of Inscuteable (insc) has been previously described to regulate the orientation of the mitotic
410 spindle during cell division. A similar activity might be present for nuclear divisions during the syncytial
411 blastoderm stage, raising the possibility that an over-expression of *mud* or *insc* could rescue embryo
412 lethality, presumably by reducing mitotic failures. However, elevated levels of neither mud nor insc
413 ameliorated high embryo lethality at 29°C (Figure S10), supporting the notion that elevated temperature
414 specifically challenges the core machinery of the mitotic spindle rather than being a non-specific failure
415 that could be rescued by any mitosis associated regulator.

416 **The natural distribution of a few regulators of spindle dynamics varies along thermoclines.**

417 While temperatures above 25°C are generally considered non-standard rearing conditions for *Drosophila*
418 lab strains, naturally occurring populations likely do experience temperatures above this presumed
419 optimum temperature. Since our analyses showed that elevated temperatures during the first hours of fly
420 development affect both, embryonic cell biology and organismal fitness, it may be tempting to predict that
421 natural populations could be adapting to temperature changes through standing genetic variation and
422 shifting allele frequencies in the same or similar genes that we identified as thermolabile regulators of
423 nuclear divisions. To address this possibility, we analyzed the distribution of standing genetic variations
424 associated with the regulators of spindle dynamics (Figure 7D) and asked whether genetic variation would
425 be distributed randomly with respect to the continent-scale gradients of annual mean temperature, i.e.
426 thermoclines. While most standing genetic variation associated with putative 'spindle dynamics' regulators

427 was indeed distributed without a clear thermoclinal pattern and did not allow for rejection of our null
428 hypothesis, (Figure 7E, Table S1), *sgg* was a clear and notable outlier in this analysis and exhibited a
429 thermoclinal distribution of natural variations independently in populations in the North America, Europe,
430 and Australia (see also, Table S2). These findings strongly suggest that the thermosensitivity that *sgg*
431 exhibits in lab conditions constitutes a biological property, which can be exposed and selected for also in
432 natural populations and during the course of evolution.

433 **Discussion:**

434 **Failing interactions between microtubules and F-actin provoke thermolability of early fly development**

435 With our work, we have characterized the processes of syncytial blastoderm formation and cellularization
436 in Drosophila embryonic development as vulnerable to elevated temperature. Embryos exposed to 29°C
437 during these stages show defects in the bilateral symmetry of development, and in extreme cases fail
438 development during gastrulation. Extreme cases of developmental failure coincide with structural defects
439 in blastoderm epithelium, which manifest as regions devoid of nuclei/cells and tissue discontinuities. These
440 discontinuities, termed blastoderm holes, stem from the clustering of mitotic failures during syncytial
441 nuclear divisions. With our analysis we show that embryonic regions, which lag behind in the nuclear
442 division cycle and exhibit nuclear crowding, produce a combinatorial predisposition for a local increase in
443 mitotic failures. We could show that mitosis itself is vulnerable at elevated temperatures due to weakened
444 interaction between microtubules and F-actin, which in turn is mediated by previously postulated tripartite
445 complex[28] between αCat, βCat, and Apc2, mediated by sgg. We speculate that exposure to elevated
446 temperature weakens the protein-protein interactions between various components of the tripartite
447 scaffold, and/or attenuate the kinase activity of sgg. Accordingly, over-expression of αCat or sgg
448 compensates for the reduced function of the complex and thus prevents the clustering of mitotic failures as
449 well as embryo lethality at 29°C. This interpretation is supported by allelic variation of sgg along
450 thermoclines, which suggests that its activity can respond to evolutionary selection pressure in wild
451 populations.

452 **Conservation of developemental defects at elevated temperature**

453 Given that early developmental processes from fertilization to blastoderm formation are overall conserved
454 across insects[31,32], our results implicate a general vulnerability in a wide range of insect species and
455 highlight a previously neglected cell biological challenge of early development in insects: the task of
456 establishing an egg cortex that is uniformly populated with cortically anchored nuclei. Loss of the uniform
457 distribution of cortical nuclei can affect positional information for subsequent steps of epithelial
458 morphogenesis and cell differentiation. Additionally, the bilateraly asymmetric nature of nuclear loss could
459 cause left-right asymmetry in the developmental processes that are otherwise symmetric, which will
460 challenge developmental robustness and increase the chances of developmental failure and embryo
461 lethality. Thus, a mechanism emerges to establish the link between the proximate effects of elevated
462 temperature on cytoskeletal regulation during mitosis, and its ultimate impact on the survival of embryos,
463 which we hypothesize to be conserved across insects.

464 In our experiments, we see weakened microtubule- F-actin interaction, leading to chromosome
465 segreagation defects. It is currently unclear whether this or other conserved mechanisms dictate the
466 defects due to elevated temperature. Assuming that such general principles may exist, we will need to
467 explore temperature dependent defects at the cellular level, with the focus on conserved cellular
468 processes, such as cellular signaling[33,34], metabolism through mitochondria[35,36], cell polarity pathways[37,38],
469 regulation of membrane trafficking[39], regulation of cell cycle[40], and cytoskeletal dynamics[41,42].

Distinction between exposure to elevated temperature and a heat shock

Previous research on *Drosophila* has shown that high temperatures trigger a "heat-shock response", which has been characterized in particular by the *de novo* transcription of genes encoding heat-shock proteins, for temperatures 33°C and higher[43]. This response has been observed in embryos[44], larvae and pupae[45,46], as well as adult flies[47]. Previous studies have used over-expression of heat-shock proteins (hsp23) to increase embryo survival in the face of a heat shock[48]. Presumably, this increases the capacitance of the system to tolerate environmental insults, akin to how heat-shock proteins are known to act as capacitors for genetic variation[49,50]. We note, however, that heat shock temperatures are present only transiently in nature[46], and might not constitute a robust selection pressure to improve tolerance to a rise in average global temperatures. Additionally, we didn't find any canonical heat-shock protein to be consistently clinal in all three continental datasets. In contrast, we observed *sgg* to exhibit allelic variation along thermoclines, showing signs of a response to selection pressure. Thus, we argue that, while the heat-shock response acts to ensure robustness against acute temperature fluctuations, it might not carry a selective advantage to build robustness at elevated temperatures. Here, the regulators of cytoskeletal interactions, however, might be targeted by natural selection, and could potentially offset the impacts of global warming. In this context, our analysis is especially crucial to identify and test candidate genes, whose expression levels could be relevant biomarkers to test for robustness of life cycle processes at elevated temperatures.

Genetically increasing robustness of early embryos against environmental perturbations

Climate change is a global challenge that threatens the existence of life on Earth as we know it[51]. Given the vital roles of flies in the functioning of ecosystems[52], insights into the effect of elevated temperature on the physiology of flies will help us understand and predict current and future adaptations of these ecosystems. Given that the early processes during embryonic development are conserved across insects[31,32], our results raise the possibility that many other insects will exhibit similar defects during early embryonic development, will have an increase in lethality, and will be overall threatened due to global warming. It is rather impressive that exposure to a sub-heat-shock elevated temperature during the first few hours of embryonic development is capable of increasing embryonic lethality: an effect which is presumably conserved across the animal kingdom, and would be worth exploring at the cellular level to improve embryo survival.

499 **Materials and methods:**

500 Fly lines and genetics:

501 *OregonR* line was used as WT *Drosophila*.

502 *Histone-RFP* expresses RFP tagged version of His2Av. Insertion on 3rd chromosome. Bloomington Drosophila
503 Stock Center (BDSC) #23650.

504 *Jupiter-GFP* expresses GFP tagged version of the microtubule-binding protein Jupiter. Insertion on 3rd
505 chromosome. Always used in combination with *Histone-RFP*. Gift from Jan Felix Evers.

506 *67-Gal4* (mat αTub-GAL4-VP16) is a maternal specific Gal4 driver. Insertion on 2nd chromosome. Always
507 used in combination with *Histone-RFP* and *Jupiter-GFP* in the over-expression experiments (see below). Gift
508 from Thomas Lecuit.

509 The following lines were used to drive the over-expression of various genes of interest in an attempt to
510 rescue the effects of 29°C. *baz*, BDSC #17613; *dlg*, BDSC #15779; *αCat*, BDSC #65590; *sgg*, BDSC #15886;
511 *mud*, BDSC #22371; *insc*, BDSC #39676. An outcross to *w1118* was used as control.

512 For various over-expression experiments, we first crossed virgins from the Gal4 line '+; 67-Gal4; Jupiter-
513 GFP, Histone-RFP' to the males of over-expression line 'UAS-X; +; +' (X= *baz*, *dlg*, *sgg*, or *mud*) or '+; +; UAS-
514 Z' (Z= *αCat*, or *insc*), or to males of *w1118* as control. F1 virgin females from these crosses were
515 backcrossed to males of the same paternal genotype.

516 Genotypes associated with various figure panels are listed in Table S3.

517 Embryo collection: For any experiment, we put males and females of appropriate genotypes (Table S3) into
518 transparent cylindrical embryo collection cages (inner diameter ~5 cm). Fine wire mesh is glued to the top
519 side of the cage to allow air exchange while keeping the flies trapped, and the bottom of the cage is closed
520 with apple-juice agar plates bearing a thin layer of yeast paste, where flies deposited the embryos. To
521 prepare the agar plates, we typically prepare 1 l of apple juice agar solution. For this, we boiled 24 gm of
522 agar in 750 ml of water, to which we added 250 ml of fresh store-bought apple juice while stirring on a hot
523 plate. We make the final amount of sucrose to 25 gm: the amount of additional sucrose depends on the
524 sugar content of the apple juice. This solution is sufficient for ~80 petri dishes of 6 cm in diameter. After
525 agar is solidified, the plates can be stored for a long time at 4°C. Before the embryo collection, the plates
526 were covered with a thin layer of yeast paste (to stimulate oviposition) and were pre-incubated to the
527 embryo collection temperature depending on the temperature regimen, for at least half an hour.
528 *Drosophila* females are known to hold onto the embryo long after fertilization, such that a large part of the
529 early embryo development can occur inside the abdomen. To avoid these embryos, we perform a sham
530 embryo collection for about an hour at room temperature (24-25°C), from which all embryos are discarded.
531 Following this sham collection, we collect the embryos that are actually used in the experiment at the
532 specific experimental temperature.

533 Embryo lethality experiment: There were 3 temperature regimes in the embryo lethality experiments, as
534 depicted in Figure 1A. Depending on the regimen, we collected embryos for 1 hour either at normal
535 temperature (24-25°C) or elevated temperature (29-30°C). The 24-25°C collections (corresponding to
536 normal temperature) were done on the bench top. The 29-30°C collections (corresponding to elevated
537 temperature) were done in a water bath, where the bottom surface of the embryo collection agar plate is
538 in thermal contact with the heated water. For NN or EN, we collected embryos for 1 hour either at normal
539 or elevated temperature and then incubated them at the same temperature for another 2 hours.
540 Afterward, the embryos are washed with bleach for 10-15 seconds, then washed thoroughly with tap

541 water, aligned on a 24x60 mm rectangular coverslip, and covered with halocarbon oil. For NE, we collected
542 embryos for 1 hour at normal temperature and then incubated them at the same temperature for another
543 1.5 hours. Within the next half an hour, the embryos are washed with bleach for 10-15 seconds, then
544 washed thoroughly with tap water, aligned on a 24x60 mm rectangular coverslip, and covered with
545 halocarbon oil. Then, we incubated them at 29°C for 3 hours. Then, for all the temperature regimen, the
546 coverslips with embryos were incubated at normal temperature for about a day, following which we
547 counted the number of eclosed larvae and the number of dead embryos. The embryonic lethality was
548 calculated as,

$$embryo\ lethality\ = \frac{100 * number\ of\ dead\ embryos}{number\ of\ dead\ embryos\ +\ number\ of\ larvae}$$

549 We excluded the unfertilized embryos from these calculations.

550 Imaging live embryos (after temperature treatment): Here we used 2 of the experimental temperature
551 regimes used in the 'Embryo lethality experiment' above, namely NN and EN. In short, we collected
552 embryos at 24-25°C (NN) or 29-30°C (EN) for 1 hour and then incubated the plate at the same temperature
553 for another 2 hours. Afterward, the embryos were washed with bleach for 35-40 sec, then washed
554 thoroughly with tap water, aligned with the dorsal side facing a 22x40 mm rectangular coverslip, covered
555 with halocarbon oil, and immediately taken for microscopy. The embryos were recorded for a variable
556 duration depending on the availability of the microscope, however, all recordings were long enough, such
557 that we could see embryonic muscle contractions in embryos that completed gastrulation. Images were
558 acquired on Leica SP8 DMi8 inverted confocal microscope using 20x glycerol objective (0.75NA), at 2 µm
559 step-size in z, and a final x-y resolution of 0.568 µm/pixel. We recorded the time-lapse at a frame rate of 1
560 frame every 4 min and recorded up to 5 embryos in parallel.

561 Imaging live embryos (at various temperatures): We used 4 experimental temperature regimes for embryo
562 live imaging. We collected embryos for 1 hour either at normal temperatures (22-23°C, 24-25°C, or 27-
563 28°C) or elevated temperature (29-30°C). The 22-23°C collections (corresponding to 22°C imaging) were
564 done in the fly incubator. The 24-25°C collections (corresponding to 25°C imaging) were done on the bench
565 top. The 27-28°C collections (corresponding to 28°C imaging) or the 29-30°C collections (corresponding to
566 29°C imaging) were done in a water bath, where the bottom surface of the embryo collection agar plate is
567 in thermal contact with the heated water. Afterward, the embryos are washed with bleach for 35-40
568 seconds, then washed thoroughly with tap water at the same temperature as embryo collection. We then
569 aligned the embryos on a 25 mm diameter circular coverslip, covered them with halocarbon oil, and
570 immediately transferred them to the temperature controller setup on the microscope that's pre-
571 equilibrated to the experimental temperatures for normal temperature regime, (22, 25, or 28°C) or the
572 elevated temperature regime (29°C). We used the temperature controller setup from Warner Instruments
573 (locally supplied by MultiChannelSystems). The setup consists of; QR-40LP, which holds the 25mm coverslip
574 with embryos; QE-1HC, which heats/cools QR-40LP along with the embryos mounted in it; LCS-1, the liquid
575 cooling system that isolates the QE-1HC from the effect of ambient temperature; and CL-100, the bipolar
576 temperature controller that can impart the temperature of interest against the baseline set by LCS-1. We
577 mounted QE-1HC on the microscope stage, with LCS-1 and CL-100 as the peripherals controlling the
578 temperature. Images were acquired on Leica SP5 DMI6000CS inverted confocal microscope using 40x water
579 objective (1.1NA), with 1x digital zoom, at 2 µm step-size in z with 20 z-steps overall, and a final x-y
580 resolution of 0.379 µm/pixel. As mentioned in the main text, we acquired images starting from interphase
581 10 or before, till the beginning of gastrulation movements. We recorded the time-lapse at a frame rate of 1

582 frame every 30 sec, 1 min, or 2 min depending on whether we recorded at a time 1, 2, or 3-4 embryos in
583 parallel.

584 Imaging fixed embryos: We used 2 different temperature regimens for embryo collection for fixation and
585 staining. We collected embryos for 3-4 hours either at normal temperature (24-25°C) or elevated
586 temperature (29-30°C). The 24-25°C collections (corresponding to the 25°C regimen) were done on the
587 bench top. The 29-30°C collections (corresponding to the 29°C regimen) were done in a water bath, where
588 the bottom surface of the embryo collection agar plate is in thermal contact with the heated water.
589 Afterwards, the embryos are washed with bleach for 40-45 seconds, washed thoroughly with tap water,
590 and fixed immediately. Collecting embryos for a longer duration is not a problem here, as we only image
591 and analyze the embryos that are before the gastrulation stage, through *post hoc* identification of the
592 developmental stage. Here, we did 2 kinds of experiments; one, where the aim was visualizing the nuclei
593 from the entire embryo (data in Figure 2); and two, where the aim was visualizing the nuclei along with F-
594 actin distributions from half embryos (data in Figure S9). Accordingly, we used 2 different protocols for
595 embryo fixation, staining, mounting, and imaging.

596 To **visualize all nuclei from the entire embryo**, we used heat fixation and stained the embryos with DRAQ5.
597 Briefly, we transferred the processed embryos to 50 ml tubes with a brush and drained the excess water.
598 To this tube, we added the boiled-to-turbidity heat-fix solution (28% 500 µl NaCl + 5% 200 µl TritonX100 +
599 19.3 ml water), incubated it for ~20 sec with thorough mixing, and then immediately added water to cool
600 down the mixture. Then, we transferred the fixed embryos to 2 ml microfuge tubes, sequentially added n-
601 heptane and methanol in equal proportions, and vigorously shook the tube for about half a minute to break
602 open and remove the vitelline membrane. This was followed by 3x washes of methanol. Here, we started
603 the staining immediately after, although the embryos can be stored in methanol for a long time. The
604 embryos were rehydrated with PBT (0.01% solution of Tween20 in PBS) over 3 washes. Following this we
605 stained the embryos with 1:1000 DRAQ5 for 1 hour. Afterward, we washed the embryos 6x with PBT, re-
606 suspended them in 3:1 glycerol:PBS solution, and mounted them between 2 rectangular coverslips. The
607 spacing between the coverslips was optimized to keep the embryos in place w/o deforming them. Then we
608 imaged the embryos through both coverslips and stitched the two half embryos during image analysis to
609 get the full view (see below). Images were acquired on Leica SP8 DMi8 inverted confocal microscope using
610 20x glycerol objective (0.75NA), with 1.15x digital zoom, at 1 µm step-size in z, and a final x-y resolution of
611 0.247 µm/pixel.

612 To **visualize the nuclei and F-actin**, we used formaldehyde fixation and stained the embryos with DAPI and
613 Phallacidin. Briefly, we transferred the processed embryos to a 20 ml vial with a brush, which contained the
614 fixation mix (3500 µl PBS + 37% 1000 µl formaldehyde + 4500 µl n-Heptane). The vial was shaken on a
615 platform shaker for 25 minutes @200 rpm. Then, we transferred the fixed embryos to 2 ml microfuge
616 tubes, sequentially added n-heptane and 90% ethanol in equal proportions, and vigorously shook the tube
617 for about half a minute to break open and remove the vitelline membrane. This was followed by 3x washes
618 of 90% ethanol. Here, we started the staining immediately after, although the embryos can be stored in
619 90% ethanol for a week or so. The embryos were rehydrated with PBT (0.01% solution of Tween20 in PBS)
620 over 3 washes, following this we stained the embryos with 1:1000 DAPI for 1 hour, followed by 1:500
621 Phallacidin for 1 hour. Afterward, we washed the embryos 4x with PBT, re-suspended them in 3:1
622 glycerol:PBS solution, and mounted them between 2 rectangular coverslips, followed by imaging. Images
623 were acquired on Leica SP8 DMi8 inverted confocal microscope using 20x glycerol objective (0.75NA), with
624 1.2x digital zoom, at 1 µm step-size in z, and a final x-y resolution of 0.473 µm/pixel.

625 Image analysis and statistics: All image analysis was done using FIJI freeware. There are 9 different kinds of
626 image analyses presented in the manuscript. These are, 1) analysis of Germband extension (live embryos),
627 2) identifying developmental landmarks (live embryos) 3) whole embryo reconstruction to visualize the
628 distribution of nuclei in the entire embryo (fixed embryos), 4) the analysis of nuclear expulsions (live
629 embryos), 5) the analysis of nuclear movements (live embryos), 6) analysis of nuclear cycle asynchrony (live
630 embryos), 7) analysis of nuclear crowding (live embryos), 8) analysis of the fraction of mitotic failures (live
631 embryos), and 9) comparing the distribution of nuclei alongside that of F-actin (fixed embryos). All the
632 statistical analysis was done using Prism (GraphPad). This includes the curve fitting (see below, the analysis
633 of nuclear crowding), estimating the non-parametric statistical significances, and estimating the 95%
634 confidence intervals (CI) on the medians. The straight-line fits for analysis of nuclear movements were done
635 using the curve fitting functions in ImageJ macro language.

636 In the **analysis of Germband extension (GBE)**, we tracked the anterior end of the posterior mid-gut (PMG)
637 to measure its distance from the posterior end. The GBE was calculated as,

$$percent\ GBE = \frac{distance\ of\ PMG\ from\ posterior * 100}{length\ of\ the\ embryo}$$

638 Plotting percent GBE against time shows the fast and slow phases of GBE.

639 In the **analysis of Developmental landmarks,** we used the following criteria to identify various
640 developmental stages and noted down the time at which these stages occurred. For *40% GBE*, we noted
641 down the time point where the anterior tip of the PMG is closest to 40% embryo length from the posterior
642 pole. For *Germband retraction begins* and *ends*, we noted down the time point when the anterior tip of the
643 elongated ectoderm on the dorsal side first moved towards the posterior and then stopped. For *head*
644 *involution*, we noted down the time point when the ectoderm meets in the anterior.

645 In the **analysis to reconstruct the nuclear distribution in the whole embryo**, we used a custom-built image
646 analysis pipeline to fuse the halves of the same embryo, followed by computing the distance of each point
647 inside the embryo from the embryo surface. Here we refer to the two views of the embryo as "half
648 embryo", even though in reality the volume in either "half" spans about 70-75% of the embryo width,
649 providing a significant overlap between the two half embryos. In the pipeline, we process the raw images,
650 stitch the two half embryos, render the fused embryo in dorsal-ventral view, segment the embryo volume,
651 and then segregate the nuclei as a function of their distance from the surface of the segmented embryo
652 volume. First, we processed the raw images: to improve visualization of the nuclei, we used a 'Minimum
653 3D' filter with radii x=y=1, and z=3, and to reduce noise, we used a 'Median 3D' filter with radii x=y=z=1.
654 Then, we homogenized the brightness/contrast between the two half embryos. Following these steps, we
655 manually aligned the half embryos along their AP axis and then used the BigWarp[53] package in the
656 BigDataViewer[54] ecosystem to align the half embryos using manually selected interest points. Essentially,
657 we selected either subcortical- or yolk-nuclei that could be identified in both half embryos. We further
658 cropped the output images to keep only a small margin around the embryo with "aligned halves", to reduce
659 the computational load in the steps to follow. After the manual alignment step, we used BigStitcher[55] to
660 further align the embryo, using the phase correlation method, to produce the "fused embryo". In the case
661 of many embryos, additional manual transforms were necessary to produce a fused embryo that passes
662 visual inspection. The fused embryos were then rotated as necessary, and resliced to produce dorsal-
663 ventral views. Following this, we processed the fused embryo to separate the regions of the embryo that
664 contain cortical-, subcortical, and yolk-nuclei. First, we used the nuclear signal to segment the embryo
665 volume, using simple thresholding. This generated a binary image that corresponds to the embryo volume.
666 Then using '3D Distance Map' (from '3DSuite' in ImageJ[56]), we compute the Euclidian distances in 3D, i.e.,

667 each pixel inside the embryo gets the grayscale value corresponding to its distance from the embryo
668 surface. All pixels with Euclidian distance <18 µm would be considered as the cortical layer, those within
669 the range of 18-45 µm would be considered subcortical, and those farther than 45µm from the embryo
670 surface would be considered as part of the yolk region (Figure 2B). These distances are determined
671 empirically, using approximate measurements from various fused embryos. The pixels in these regions
672 were then color-coded and presented as maximum projections in Figure 2.

673 In the **analysis of nuclear expulsions**, we tracked expelled nuclei back in time to identify the mitosis when
674 they were born and to categorize the expulsion as isolated (Figure 3A, B) or pairwise (Figure 3E). We
675 considered a nucleus to be expelled if its apical-most tip was at least 12 µm away from the embryo surface.
676 To simplify the identification of expelled nuclei, we color-coded the Histone-RFP signal as a function of
677 distance from the embryo surface. This is similar to above analyses, except we use the 'LocalZPojector'
678 plugin[57] in FIJI to define the distance from the embryo surface, while to predict the embryo surface itself we
679 use the Jupiter-GFP signal, which was co-imaged with Histone-RFP. Thus, first, we color-code the nuclei,
680 and then manually identify and count the number of pairwise or isolated nuclear expulsions.

681 In the **analysis of nuclear movements**, for a select few nuclei, we manually tracked the entire progeny,
682 starting from the mother nucleus in late interphase 10 till the 8 great-granddaughter nuclei in late
683 interphase 13. Assigned all of these nuclei to a single cluster, we then calculated the center of the cluster at
684 each time point. We chose nuclei along one continuous row at interphase 10 and tracked their progeny in
685 their clusters. For the sake of simplicity and consistency, we only chose those nuclear clusters whose entire
686 progeny could be tracked, i.e., we could follow the cluster and see the formation of all 8 great-
687 granddaughter nuclei in interphase 13. This way, we obtained ≥ 13 clusters in any embryo that we tracked.
688 For each of these nuclear cluster trajectories, we fitted a straight line to coordinates for the center of the
689 cluster, over time (dashed lines in Figure S4B). Then, we calculated the distance of the center of the nuclear
690 cluster to this line at every time point. An average of these distances over a specific period was used as an
691 estimate for deviations in the center of nuclear clusters over that period. We observed that the clusters
692 move significantly starting from anaphase till a few minutes into the subsequent interphase, as the clusters
693 return to their normal position. Thus, we decided to separately analyze these periods of extensive
694 movement vs. the periods when the cluster movement was low. To identify the periods of extensive
695 movements consistently and objectively, we noted that these movements start at least 1 timepoint (30 sec)
696 before we could see the first telophase in any of the tracked clusters, while the movements mostly subside
697 within 3 minutes after all of the nuclear clusters finished telophase. Thus, we defined the window of
698 extensive movement as starting from 30 sec before the appearance of the first telophase nuclei, till 3 min
699 after the appearance of the last telophase nuclei. Once we had an objective definition of various periods, it
700 was straightforward to calculate the average deviation in the center of nuclear clusters.

701 In the **analysis of asynchrony in nuclear cycles**, we marked various time points in the timelapse recordings
702 to follow the progression of nuclear cycles in the anterior-, middle-, and posterior-5th of the field of view.
703 For the sake of simplicity, we marked the transitions from a telophase 13 to interphase 14, i.e., the first
704 time point when the daughter nuclei in any region go from telophase 13 to interphase 14. If the timepoint
705 for this occurrence in the anterior is 'T_a', that in posterior is 'T_p', while the same in the middle is 'T_m', then
706 the 'asynchrony' can be calculated as,

$$asynchrony = T_m - \left(\frac{T_a + T_p}{2}\right)$$

707 Essentially, we started with the expectation that T_m should be the average of T_a and T_p (maximum
708 synchrony), and a deviation from this expected value would be the asynchrony.

709 In the **analysis of nuclear crowding**, we analyzed the distribution of nuclei at the end of interphases, as
710 that's the time when the distribution is as stable as it can be, with maximum crowding, if any. To assess
711 nuclear crowding, we started with the segmentation of nuclei in the field of view. Here, we used the 'Find
712 Maxima' command to identify local intensity maxima and imprinted those on an image. Many of these
713 maxima marked a nucleus. We did manual corrections to, remove the maxima that didn't correspond to a
714 nucleus, add a maximum for nuclei that didn't have a maximum associated with them, or correct the
715 maxima that were too off-center from the corresponding nucleus. Then we used Voronoi tessellation to
716 mark territories around these maxima to generate pseudo-cells. We excluded territories that, touched the
717 edge of the image, that had aberrant shapes (aspect ratio>2), or those with aberrant pixel intensities
718 (pseudo cells containing pixels with <5 units of intensity, typically the case with ill-defined pseudo-cells at
719 the edge of segmentation). Thus, each nucleus was associated with a pseudo-cell area value ('Area' in μm^2),
720 and an x-coordinate value for the center of the pseudo-cell ('X' in µm) (x-axis of the image aligned with the
721 anterior-posterior axis of the embryo). We fitted these with the equation of a parabola such that 'Area' can
722 be expressed as a function of 'X',

$$Area = aX^2 + bX + c$$

723 Here, the curvature of the parabola will be higher in case of greater nuclear crowding (compare Figure 5I-L).
724 Thus, the fit parameter 'a', which dictates the curvature of the parabola, was used to estimate the extent of
725 crowding.

726 In the **analysis of the fraction of mitotic failures**, we tracked expelled nuclei back in time same as the
727 analysis for mitotic failures, except now we also recorded where the nuclei were lost from, to get a map of
728 the locations of mitotic failure in the field-of-view. In parallel, we generated regions in the embryo that
729 correspond to maximum nuclear crowding, maximum delay in nuclear divisions, and a combination of the
730 two regions. To construct the <u>crowded regions</u> (the region corresponding to maximum nuclear crowding)
731 we referred to previous studies, which have argued that a certain threshold of nuclear content will halt the
732 syncytial nuclear division cycles[58]. This threshold was determined to be ~70% of the normal cellularization
733 nuclear density[59]. Here, we argue that such threshold nuclear content is reached in regions with nuclear
734 crowding, albeit only locally, and should locally trigger an arrest of nuclear divisions, in conflict with the rest
735 of the embryo. Another previous study reported the nuclear domain area (i.e., the pseudo-cell area) to be
736 28.8 μm^2 at cellularization[60]. We corroborated this number with our own quantifications (data not shown).
737 For simplicity of calculations, we assumed that *Drosophila* embryos have 6000 nuclei at interphase 14 each
738 with an area of 29 μm^2. The 70% density of nuclei would thus correspond to 4200 nuclei at interphase 14,
739 each with an area of 41.43 μm^2, which we approximated to 42 μm^2. This back-of-the-envelop calculation
740 indicated that nuclei will seize to divide when their pseudo-cell area drops below ~42 μm^2. We observed
741 that in embryos developing at 29°C, the central regions of the embryo contained many nuclei that had
742 pseudo-cell areas less than 42 μm^2, already at interphase 13. Thus, we used this criterion to define areas of
743 embryos that have likely reached the 70% cellularization nuclear density, at one nuclear division cycle
744 earlier, albeit only locally. Since the embryos at normal temperatures (22, 25, and 28°C) rarely have nuclei
745 with pseudo-cell areas smaller than 42 μm^2, we further decided to include all nuclei with pseudo-cell areas
746 in the lower quartile to construct the region with maximum nuclear crowding. Here we also note that this
747 description is only a rationalization of the approach and that it is not a comment on how the effect of
748 nuclear crowding might actually manifest. For instance, it is also likely that mitotic spindles are not properly
749 established in crowded regions, thus causing mitotic failure. However, this wouldn't allow us to define
750 equivalent regions in the embryos at normal temperatures, as it is not feasible to accurately define the size
751 of the mitotic spindle, in our experiments. Moreover, it is quite likely that we need a certain threshold size
752 of the crowded region to actually prevent mitosis, thus we might still see divisions in nuclei that have a

753 pseudo-cell area smaller than 42 μm^2. Then, to construct the delayed region (the region with maximum
754 delay in nuclear divisions), we simply marked the areas of the embryo that contain the last ~20% of the
755 nuclei that finished nuclear cycle 13. This percentage was decided empirically: it corresponds to a region of
756 similar size as that corresponding to the crowded regions above. Here the rationale is drawn from previous
757 studies which indicate that the regulation of nuclear division cycles is coordinated at the scale of the entire
758 embryo [24], and given that all of the nuclei share the same cytoplasm, a local delay in nuclear cycles would
759 create conflicts between the biochemical status of the cytoplasm and the cell cycle stage of the delayed
760 nuclei. Finally, to construct the combined region (combination of crowded and delayed region), we used
761 the logical OR operator to combine the crowded and delayed regions, to test the combinatorial effects of
762 the nuclear crowding and nuclear cycle asynchrony. In the end, we computed the fraction of mitotic failures
763 in the crowded, delayed, or combined regions using,

$$fraction\ of\ mitotic\ failures = \frac{number\ of\ mitotic\ failures\ in\ a\ specific\ region}{total\ number\ of\ mitotic\ failures}$$

764 In the **analysis to compare the distribution of nuclei alongside that of F-actin**, was rather similar to the
765 pipeline to *reconstruct the nuclear distribution in the whole embryo*, except that we didn't have 2 half-
766 embryos to fuse, essentially starting from segmentation of embryo volume. Here, instead of using nuclear
767 staining, we segmented embryo volume using the F-actin staining. Then the 3D distance map similarly
768 allowed us to classify pixels into cortical-, subcortical-, or yolk regions based on their distance from the
769 embryo surface. The pixels in these regions were then color-coded and presented as sum projections in
770 Figure S9.

771 **Figure and table legends:**

772 **Figure 1: Embryonic lethality and developmental defects in embryos exposed to elevated temperature.**

773 (A, B) To assess developmental robustness, we exposed embryos to various temperature regimen and
774 estimated the embryo lethality. (A) Schematic showing the temperature regimen in the embryo survival
775 experiment. Here we have three conditions depending on exposure to normal or elevated temperature
776 regimen in the 3-hour time windows as shown, normal-normal [NN], elevated-normal [EN], and normal-
777 elevated [NE]. In all cases, the first time window also includes 1 hour of embryo collection, and the
778 embryonic development beyond 6 hours continued at normal temperature. (B) The scatter plots show the
779 distribution of the percentage of embryos that don't hatch into larvae. Each dot represents data from a
780 sample with ≥26 embryos; n= 12 (NN), 10 (EN), 10 (NE) samples.

781 (C-E) Montages of snapshots from live embryos, expressing Histone-RFP, from early gastrulation till late
782 gastrulation, in embryos developing at 25°C. Till the late cellularization stage, these embryos were exposed
783 to either 25°C, i.e., NN temperature regimen (C), or 29°C, i.e., EN temperature regimen, showing mild (D),
784 or severe (E) defect. White dashed lines indicate the dorsal midline drawn based on the egg shape, while
785 the red dashed line marks the embryonic midline in the dorsal posterior ectoderm. Orange dashed lines
786 indicate the anterior end of the posterior mid-gut to mark the extent of the Germband extension.

787 (F) Plot showing the extent of Germband extension (GBE) with the hollow markers indicate embryos that
788 have defects during gastrulation. These embryos are excluded from further analysis of developmental
789 landmarks. (G) The analysis of Developmental landmarks shows the time at which various events can be
790 seen in the embryos. Time points from individual embryos are plotted at the same y-value.

791 Scale bar, 50 µm. B show scatters with median, with whiskers showing 95% CI. *, $p<0.05$; **, $p<0.01$; ***,
792 $p<0.001$; ****, $p<0.0001$, non-significant comparisons are not shown.

Figure 2: Nuclear loss shows left-right asymmetry in embryos developing at elevated temperature.

(A) Pie charts showing the occurrence of blastoderm holes during cellularization in fixed embryos that were developing either at normal temperature (n=68) or elevated temperature (n=77). Here, a blastoderm hole is defined as a cluster of >10 subcortical nuclei, with a corresponding discontinuity in the cortical layer of nuclei.

(B) Schematic shows various layers of the embryo volume, where green indicates region of cortical nuclei, i.e., nuclei within 18 µm from embryo surface; magenta indicates region of sub-cortical nuclei, i.e., nuclei that are deeper than 18 µm till a depth of 45 µm in the embryo; and yellow indicates the region of yolk nuclei (vitellophages) that are found at a depth of >45 µm.

(C-H) Distribution of nuclei in embryos during interphase 14, in fixed embryos that were developing either at normal temperature (C, F) or at an elevated temperature that shows either a mild defect (D, G) or a severe defect (E, H). Here the top/bottom panels show the maximum intensity projections in dorsal/ventral halves of the embryos, with white/gray dashed lines indicating respective midlines drawn based on the egg shape. Here the voxels are color-coded as a function of their distance from the embryo surface as shown in B. Embryo orientation is consistently presented in all panels and is indicated in C. (C-E) Cortical and subcortical nuclei are shown, where embryos at normal temperature (C) show rarely any gaps, while those at elevated temperature show small (D) or large (E) gaps in the distribution of cortical nuclei. These gaps often also correspond to the locations of subcortical nuclei. (F-H) The corresponding subcortical nuclei are shown separately for improved visibility, along with yolk nuclei.

Scale bar, 50 µm.

Figure 3: Nuclear loss as isolated or paired expulsions at elevated temperature.

(A-D) To assess isolated nuclear expulsions, we followed them back to either out-of-plane divisions (A, C) or in-plane divisions (B, D). (A) Montages exemplify out-of-plane division during mitosis 10 in an embryo developing at 25°C. Histone-RFP marks the nuclei (green), while Jupiter-GFP marks the microtubules (magenta). Arrowheads/arrows exemplify in-plane/out-of-plane division. Each subsequent frame is 1 minute apart. In the x-y view of the divisions (A, top panels), only one of the daughter nuclei is visible after the out-of-plane division, while the other daughter nucleus is better seen in the y-z view of the division (A, bottom panels), as it translocates to the embryo interior. White lines outline the embryo surface in Y-Z views. (B) Montage exemplifying in-plane divisions in an embryo developing at 25°C, from telophase 12 to late interphase 13. Histone-RFP marks the distribution of nuclei, cortical nuclei are in green, and subcortical (lost) nuclei are in magenta, as shown in the schematic. The arrowheads/arrows track the daughter nucleus that will be expelled/cortically retained. (C) Scatter plot showing the number of out-of-plane divisions, that are visible in the field of view, in embryos developing at various temperatures. For context, an embryo contains on the order of 70 mitotic spindles in the field of view at mitosis 10. So, even though the p-value is <0.05 for the comparison between 22°C and 29°C, we would argue that the difference is not biologically significant, given that there is no correlation between the number of out-of-plane divisions and the presence of blastoderm holes. (D) Scatter plots showing the number of isolated loss of nuclei during interphase 14 after in-plane divisions.

(E-G) To assess the pairwise loss of nuclei, we counted mitotic failures that led to such nuclear expulsions. (E) Montage of snapshots from the live embryo, from late interphase 12 to late interphase 13, where Histone-RFP marks the distribution of nuclei, cortical nuclei are in green, and subcortical (lost) nuclei are in magenta, same as shown in the schematic in B. The pairwise loss of nuclei due to mitotic failure is exemplified in an embryo developing at 29°C. The arrowheads track the segregating daughter nuclei that

836 will be expelled eventually, while arrows exemplify normal nuclei. (F) Scatter plot showing the number of
837 pairwise nuclear expulsions observed during interphase 14. (G) The schematic illustrates the phenomenon
838 of mitotic failures at elevated temperature.

839 Scale bars; A, 10 µm; B and E, 5 µm. C, D, and F show scatters with median, with whiskers showing 95% CI.
840 Hollow markers indicate embryos that have a blastoderm hole, with large hollow markers indicating a
841 single large hole, and small hollow markers indicating either a single or multiple small holes. n= 10 (22°C), 7
842 (25°C), 9 (28°C), and 10 (29°C) embryos. *, p<0.05; **, p<0.01; non-significant comparisons are not shown.

843 **Figure 4: Nuclear cycle asynchrony increases as a function of temperature during embryo development.**

844 To assess the asynchrony in nuclear cycles, we identified the phases of the nuclear cycle along the AP axis.
845 (A, B) Image shows the entire anterior-posterior extent of the field of view, from a live embryo developing
846 at 25°C (A) and 29°C (B). Histone-RFP marks the nuclei, cortical nuclei are in green, and subcortical (lost)
847 nuclei are in magenta. Different regions of the embryo have nuclei in different stages of the nuclear division
848 cycle, as indicated above in the image. Arrows show the direction in which the wave of the nuclear division
849 cycle will progress. At 25°C, we see a single wave from the anterior, while we see an anterior- and a
850 posterior-wave at 29°C. (C) Scatter plots showing the asynchrony for embryos at various temperatures. n=
851 10 (22°C), 7 (25°C), 9 (28°C), and 10 (29°C) embryos. (D) The schematic illustrates the progressive increase
852 in asynchrony at elevated temperature.

853 Scale bars, 20 µm. C shows scatters with median, with whiskers showing 95% CI. Hollow markers indicate
854 data from embryos that have blastoderm holes, with large hollow markers indicating a single large hole,
855 and small hollow markers indicating either a single or multiple small holes. *, p<0.05; **, p<0.01; ***,
856 p<0.001; non-significant comparisons are not shown.

857 **Figure 5: Nuclear crowding increases as a function of temperature during embryo development.**

858 (A-L) To assess the crowding of nuclei, we segmented the nuclei and generated pseudo-cells. The figure
859 shows data from representative live embryos that were developing either at 22°C (A, E, I), 25°C (B, F, J),
860 28°C (C, G, K), or at 29°C (D, H, L). (A-D) Snapshots from live embryos at the end of interphase 13, where
861 Histone-RFP marks the nuclei. The outline shows the region of the image that is considered for
862 quantifications. (E-H) The pseudo-cells for the corresponding embryos in A-D. The region of a pseudo-cell is
863 bound by line segments that are equidistant from neighboring nuclei. Various pseudo-cells are color-coded
864 according to their area in μm^2 according to the LUT at the bottom. (I-L) Plots showing the distribution of
865 pseudo-cell areas as a function of their anterior-posterior position, along with a quadratic fit through the
866 distribution, for corresponding embryos in A-D.

867 (M) Scatter plots showing the distribution of the coefficient of the quadratic term for embryos at various
868 temperatures. This essentially captures the extent of nuclear crowding, with a larger quadratic coefficient
869 indicating greater crowding. n= 10 (22°C), 7 (25°C), 9 (28°C), and 10 (29°C) embryos. (N) The schematic
870 illustrates the crowding effect at elevated temperature. The size of the black arrows indicates the gradation
871 in nuclear density, from poles to the central region.

872 Scale bars, 20 µm. M shows scatters with median, with whiskers showing 95% CI. Hollow markers indicate
873 data from embryos that have blastoderm holes, with large hollow markers indicating a single large hole,
874 and small hollow markers indicating either a single or multiple small holes. *, p<0.05; **, p<0.01; ***,
875 p<0.001; non-significant comparisons are not shown.

876 **Figure 6: Nuclear crowding and nuclear cycle asynchrony combinatorially enhance mitotic failure defect.**

877 (A, B) Snapshots from live embryos, developing at 29°C, at the end of interphase 13 (A), and 14 min
878 afterwards (B), where Histone-RFP marks the nuclei. The outline in A shows the region of the image that
879 has nuclear crowding, while that in B shows the region containing the most delayed nuclei, i.e., those that
880 are most lagging in nuclear division cycles.

881 (C-H) The locations of lost pairs of nuclei during interphase 14 are marked as white dots to indicate their
882 distribution in the field of view. Then, various regions are defined in the embryo to illustrate the fraction of
883 mitotic failures occurring in that region. These regions are composed based on, the crowded region (C), the
884 delayed region (D), and the combined region (E). (F-H) Scatter plots showing the distribution of the fraction
885 of mitotic failures occurring in the crowded (F), delayed (G), and combined (H) regions of the embryos.

886 Scale bars, 20 µm. F-H show scatters with median, with whiskers showing 95% CI. Hollow markers indicate
887 data from embryos that have blastoderm holes, with large hollow markers indicating a single large hole,
888 and small hollow markers indicating either a single or multiple small holes. n= 10 (22°C), 7 (25°C), 9 (28°C),
889 and 10 (29°C) embryos. *, p<0.05; **, p<0.01; non-significant comparisons are not shown.

890 **Figure 7: Rescue of embryonic lethality at elevated temperature through over-expressions, and clinal**
891 **genes as "natural" candidates.**

892 (A-C) Testing the rescue of embryonic lethality and the fraction of mitotic failures with over-expression of
893 *Cat* or *sgg*. (A) Scatter plot showing the distribution of percent lethality in embryos from various
894 genotypes, at normal (25°C) vs elevated temperature (29°C), calculated based on the fraction of embryos
895 that don't hatch into larvae. Each dot represents data from a sample with ≥18 embryos; control, n= 10
896 (25°C), 11 (29°C) samples; Cat-OE, n= 10 (25°C), 12 (29°C) samples; sgg-OE, n= 8 (25°C), 7 (29°C) samples.
897 Scatter plots showing the distribution of the fraction of mitotic failures in crowded regions (B), and in
898 crowded OR delayed regions (C), in the embryos at normal (22°C) vs elevated temperature (29°C). Each dot
899 represents data from one embryo: control, n= 8 (22°C), 9 (29°C) embryos; Cat-OE, n= 8 (22°C), 8 (29°C)
900 embryos; sgg-OE, n= 7 (22°C), 7 (29°C) embryos.

901 (D, E) Analysis of "natural" candidate genes that vary along thermoclines. (D) Venn diagram illustrates how
902 we constructed a non-redundant list of genes associated with 'spindle dynamics' through the union of
903 genes associated with GO terms, cell polarity (n=203 genes), spindle localization (n=37 genes), and spindle
904 organization (n=138 genes). (E) Pie charts showing the clinal distribution score for various genes associated
905 with 'spindle dynamics' as constructed in G (n=320 genes), or with GO term 'metabolic process' (n=6612
906 genes). ~1% of genes associated with 'spindle dynamics', while ~0.2% of the genes associated with
907 'metabolic process', are clinal in all three continental datasets. See also, Tables S1 and S2.

908 A-C shows scatters with median, with whiskers showing 95% CI. In B and C, hollow markers indicate data
909 from embryos that have blastoderm holes, with large hollow markers indicating a single large hole, and
910 small hollow markers indicating either a single or multiple small holes. *, p<0.05; **, p<0.01; ***, p<0.001;
911 ****, p<0.0001; non-significant comparisons are not shown.

912 **Figure S1: Nuclei are expelled in embryos at elevated temperature.**

913 (A-C) Montages of snapshots from live embryos, expressing Histone-RFP, from late interphase 11 till late
914 interphase 14, in embryos developing either at normal temperatures (A), or at elevated temperature
915 showing mild (B), or severe (C) defect. The nuclei were labeled as a function of their distance from the
916 embryo surface. Here, green indicates cortical, and magenta indicates sub-cortical nuclei that are lost. At
917 elevated temperature, a lot more nuclei are expelled, and as a result, we can see large gaps between
918 cortical (green) nuclei, often coinciding with expelled (magenta) nuclei, especially during early interphase-
919 14.

Scale bars, 25 µm.

Figure S2: Blastoderm holes appear in a fraction of embryos at elevated temperature.

The figure shows the snapshots from live embryos, expressing Histone-RFP, from early interphase 14, in embryos developed at elevated temperature. The nuclei are labeled as a function of their distance from the embryo surface. Here, green indicates cortical, and magenta indicates sub-cortical nuclei that are expelled, while arrows/arrowheads indicate large/small blastoderm holes. For embryos with large blastoderm holes (embryos 05, and 08), we see many nuclei in magenta. In contrast, in the case of embryos with small blastoderm holes (embryos 04, and 09), we can see only a few nuclei in magenta per hole. We would argue that development in *Drosophila* is robust enough to buffer the defects due to the small holes, but fails at 29°C when large holes appear.

Scale bar, 25 µm.

Figure S3: Defective nuclei take different amounts of time to be expelled from the embryo cortex.

(A, B) The figure shows the montages of snapshots from live embryos, with a few representative nuclei tracked from late interphase 12 to interphase 13. The top panels show Histone-RFP signal, while the bottom panels show Jupiter-GFP signal. Nuclei tagged in green/magenta are the ones that arise from mitotic defects during mitosis 10/11. All of these are expelled during interphase 13. Notice the lack of spindle formation around the tagged nuclei. Also, note that the nuclei expelled by the 5th timepoint are not shown in the 6th timepoint. (A) An embryo developing at normal temperature, where 1 magenta and 1 green nuclei are followed. (B) An embryo developing at elevated temperature, where 6 magenta and 3 green nuclei are followed.

Scale bars, 20 µm. The numbers in the inset indicate time in min:sec.

Figure S4: Nuclear movement parallel to the embryo surface is amplified at elevated temperature.

(A-C) An example depicting how the nuclear movements are tracked, and the deviations thereof are calculated. Snapshots from live embryo developing at elevated temperature, where Histone-RFP marks the distribution of nuclei, showing the mother nuclei at the end of interphase 10 (A) and the corresponding 8 great-granddaughter nuclei, each, at the end of interphase 13 (C). The neighboring nuclear clusters are marked in either cyan or yellow. The trajectories of the center of nuclear clusters (B) also indicate the increase in the number of nuclei due to divisions, as the broadening of the tracks. The dotted lines indicate straight lines fitted to individual trajectories, which are used as reference for computing deviations for each time point of that trajectory. The shaded region captures periods of greatest movement that start with anaphase (see methods).

(D-I) To quantify the drift in the center of nuclear clusters, we compute the slope of the straight-line fits (dotted lines in B). The median of slopes for all nuclear clusters from one embryo provides a robust estimate of the drift in the centers of the nuclear clusters. Plots showing the distribution of these medians (one dot per embryo), for the drift along the AP axis (D), and that along the DV axis (E). To quantify the movements in the center of nuclear clusters during periods of maximum movement (shaded region in B) and normal movement (unshaded regions in B), we compute the average of the deviations from the straight-line fits (dotted lines in B). The median of such average deviations for all nuclear clusters from one embryo provides a robust estimate of the nuclear cluster deviation. Plots showing the distribution of these medians (one dot per embryo), for the fluctuations along the AP axis (F, H), and those along the DV axis (G, I), during interphase-metaphase (F, G) or anaphase-telophase (H, I).

Scale bar, 25 µm. D to I show scatters with median, with whiskers showing 95% CI. Hollow markers indicate data from embryos that have blastoderm holes, with large hollow markers indicating a single large hole, and small hollow markers indicating either a single or multiple small holes. n= 10 (22°C), 7 (25°C), 9 (28°C), and 10 (29°C) embryos. *, p<0.05; **, p<0.01; ***, p<0.001; non-significant comparisons are not shown.

Figure S5: Nuclear movement along surface-yolk axis is amplified at elevated temperature.

Cross-sections from live embryos, expressing Histone-RFP, from late interphase 13 till early interphase 14, in embryos developing either at normal temperature (A) or at elevated temperature (B). Here, the colored lines mark the basal tip of nuclei in the first frames (t=-7:30 min) of the respective montage. Timepoint 00:00 corresponds to the initiation of anaphase at the left/right extreme of the images, which is also the first time we see the shift from baseline in embryo at elevated temperature.

Arrowheads point out the local peak of the nuclear shift from the baseline, while arrow points expelled nuclei. As we can see, at elevated temperature, the nuclei shift significantly from the baseline, before returning to normal localization by the time the nuclei enter the subsequent interphase. Also, the shift from baseline occurs progressively from the anterior/posterior poles towards the central region.

Scale bars, 25 µm. Cross-sections are in the lateral region of the embryos, anterior to the left.

Figure S6: Nuclear cycle asynchrony increases as a function of temperature during embryo development.

To assess the asynchrony in nuclear cycles, we identified the phases of the nuclear cycle along the AP axis. (A, B) Montages of snapshots at the transition from nuclear cycle 13 to early interphase 14, from live embryos developing either at 25°C (A), or at 29°C (B). Histone-RFP marks the nuclei, cortical nuclei are in green, and subcortical (lost) nuclei are in magenta. The anterior, central, and posterior 1/5th of the field of view are as indicated. Numbers in the inset represent time in min:sec, while 00:00 is when the anterior 1/5th of the embryo enters interphase 14. Boxes highlight entry into interphase 14 in that region.

Scale bars, 20 µm.

Figure S7: Area fractions don't explain the trends in fraction of mitotic failures.

(A-C) Scatter plots showing the distribution of the area fractions in crowded (A), delayed (B), and combined (C) regions of the embryos. In the case of both crowded (A) and delayed (B) regions, the medians are rather comparable across temperatures, and the low variability within a given temperature exaggerates the differences across temperatures. In the case of the area fraction of the combined regions (C), the increase in the overlap of crowded and delayed regions reduces the overall size of the combined regions.

Plots show scatters with median, with whiskers showing 95% CI. Hollow markers indicate data from embryos that have blastoderm holes, with large hollow markers indicating a single large hole, and small hollow markers indicating either a single or multiple small holes. n= 10 (22°C), 7 (25°C), 9 (28°C), and 10 (29°C) embryos. *, p<0.05; **, p<0.01; ***, p<0.001; non-significant comparisons are not shown.

Figure S8: Rescue of embryonic lethality at elevated temperature through *baz* or *dlg* over-expressions.

(A-C) Testing the rescue of embryonic lethality and the fraction of mitotic failures with over-expression of *baz* and *dlg*. (A) Scatter plot showing the distribution of percent lethality in embryos from various genotypes, at normal (25°C) vs elevated temperature (29°C), calculated based on the fraction of embryos that don't hatch into larvae. Each dot represents data from a sample with ≥12 embryos; control, n= 9 (25°C), 9 (29°C) samples; baz-OE, n= 11 (25°C), 10 (29°C) samples; dlg-OE, n= 12 (25°C), 10 (29°C) samples. Scatter plots showing the distribution of the fraction of mitotic failures in crowded regions (B), and in crowded OR delayed regions (C), in the embryos at normal (22°C) vs elevated temperature (29°C). Each dot

represents data from one embryo: control, n= 7 (22°C), 9 (29°C) embryos; baz-OE, n= 7 (22°C), 7 (29°C) embryos; dlg-OE, n= 6 (22°C), 7 (29°C) embryos.

Plots shows scatters with median, with whiskers showing 95% CI. In B and C, hollow markers indicate data from embryos that have blastoderm holes, with large hollow markers indicating a single large hole, and small hollow markers indicating either a single or multiple small holes. *, p<0.05; **, p<0.01; ***, p<0.001; non-significant comparisons are not shown.

Figure S9: Elevated temperature disrupts the association between nuclei and F-actin caps.

Distribution of nuclei and F-actin in embryos during interphase 13, in fixed embryos that were developing either at normal temperatures (A, C, D), or elevated temperature (B, E, F). (A, B) The images show SUM projections of the DAPI-stained nuclei (top image) and Phallacidin-stained F-actin (bottom image) of representative embryos. In the top images, the nuclei are labeled as a function of their distance from the embryo surface, where green indicates cortical, and magenta indicates sub-cortical nuclei. The yolk nuclei are not shown. Anterior is on the left, dorsal up. (C-F) The top and bottom images show a zoomed-in view of the indicated regions in panels A and B. Here, arrowheads indicate the expelled nuclei (C, E top panels) and the gaps between the actin-caps of neighboring nuclei (C, E bottom panels). Then, the arrows indicate gaps between neighboring nuclei (D, F top panels), where we can see gaps between the actin-caps of neighboring nuclei (D, bottom panel), but contain small "actin caps" in embryos at elevated temperature (F, bottom panel).

Scale bars, 25µm. The boxed regions are 60x60 µm.

Figure S10: *mud* or *insc* over-expression does not ameliorate embryo survival at elevated temperature.

Scatter plot shows the distribution of percent lethality in embryos from various genotypes, at normal (25°C) vs elevated temperature (29°C), calculated based on the fraction of embryos that don't hatch into larvae. Each dot represents data from a sample with ≥21 embryos; control, n= 10 (22°C), 11 (29°C) samples; mud-OE, n= 11 (22°C), 12 (29°C) samples; insc-OE, n= 7 (22°C), 10 (29°C) samples. As we can see in the plot, neither *mud* nor *insc* over-expression rescues the embryo lethality at elevated temperature, with *mud* over-expression increasing embryo lethality even at normal temperature (25°C).

The plot shows scatters with a median, while whiskers show 95% CI. *, p<0.05; **, p<0.01; ***, p<0.001; non-significant differences are omitted.

Table S1: This table contains genes that are identified as being clinal in different continents. Columns A to C contain lists of studies, and under the studies is a list of genes that are identified in these studies as being clinal. Columns A, B, and C respectively list studies that have data from the continents of Australia and/or Australasia (AUS) [61–70], North and/or Central America (USA) [61,68,78–80,70–77], and Europe and/or North Africa (EU) [61,67,81,82]. We collect all the genes associated with 'spindle dynamics' (Figure 7D), to compile a list of potential candidate genes in Column F. For each gene in column F, we count the number of times that gene appears in columns A to C, counting a maximum of once per column, to respectively populate columns G to I. For each gene in column F, column J contains the sum of values in G, H, and I, to indicate the number of continents in which a gene is clinal. Each gene gets a score from 0 to 3, and we consider the gene to be a relevant candidate if it is found in at least 2 columns, i.e., with a score of 2 or 3.

We collect all the genes associated with the GO term 'metabolic process', to compile a control list of candidate genes in Column L. For each gene in column L, we count the number of times that gene appears in columns A to C, counting a maximum of once per column, to respectively populate columns M to O. For

each gene in column L, column P contains the sum of values in M, N, and O, to indicate the number of continents in which a gene is clinal. Thus, each gene gets a score from 0 to 3.

Table S2: Column A lists candidates from Table S1 column F that have a score of 2 or higher, i.e., those that show significant selectable variation in natural populations. For these genes, we query FlyBase (http://flybase.org/batchdownload) for additional details like gene name (column B), gene symbol (column C), and the level of expression during the first 2 hours of embryo development (column D). The level of expression is based on published transcriptomics data[83], which would correspond to a maternal pool of mRNAs, the most relevant developmental window for this study. The candidate genes clinal in all 3 continents are highlighted in green. Columns F-J present a table with counts of genes that are associated with various categories of genes in Table S1 columns F and L, and a further breakdown of how many of these genes are clinal in how many continents. The breakdown is also plotted as pie charts in Figure 7E.

Table S3: This table lists various figure panels (columns A and B), and the related parental genotypes, i.e., the genotypes of females (column C) and males (column D) present in the embryo collection cages for the experiment related to a figure panel.

Additional information

Data and Code Availability: Data and codes developed for data analysis are available upon request from corresponding authors.

Author contributions: G.K. and S.L. planned the project. G.K. did the experiments with help from P.A. for baz and dlg overexpressions, JJ.D.-L. for nuclei, and F-actin staining. G.K. did the image analyses and statistical analyses. G.K. and S.L. wrote the manuscript, and all authors gave comments on the manuscript.

Acknowledgments: We would like to thank Lázaro Centanin, Nicolas Gompel, and Marianthi Karageorgi for insightful comments on various drafts of the manuscript, and Lemke lab members for discussions throughout the project. We are grateful to Jochen Wittbrodt for his enthusiasm and his continuous and generous support. We would also like to thank Ingrid Lohmann for *Drosophila* culture-related support, and Thomas Lecuit for sharing fly lines. We sincerely appreciate the efforts taken by FlyBase to maintain a curated database and Bloomington Drosophila Stock Center for providing transgenic fly lines. This work was funded by the DFG (LE 2787/3-1) to S.L., while G.K. was supported through an HFSP Long-term postdoctoral fellowship (LT000597/2019-L).

Competing interests: The authors declare no competing financial interests.

References:

1. Wiens, J.J. (2016). Climate-Related Local Extinctions Are Already Widespread among Plant and Animal Species. PLoS Biol. *14*, e2001104. 10.1371/journal.pbio.2001104.
2. Edwards, M.J. (2006). Review: Hyperthermia and fever during pregnancy. Birth Defects Res. A. Clin. Mol. Teratol. *76*, 507–516. 10.1002/bdra.20277.
3. Miller, M.W., and Church, C.C. (2013). Arrhenius thermodynamics and birth defects: chemical teratogen synergy. Untested, testable, and projected relevance. Birth Defects Res. C. Embryo Today *99*, 50–60. 10.1002/bdrc.21025.
4. Graham, J.M. (2020). Update on the gestational effects of maternal hyperthermia. Birth defects Res. *112*, 943–952. 10.1002/bdr2.1696.
5. Cockroft, D.L., and New, D.A.T. (1978). Abnormalities induced in cultured rat embryos by hyperthermia. Teratology *17*, 277–283. 10.1002/tera.1420170306.
6. Germain, M. -A, Webster, W.S., and Edwards, M.J. (1985). Hyperthermia as a teratogen: parameters determining hyperthermia-induced head defects in the rat. Teratology *31*, 265–272.

1086 10.1002/tera.1420310212.
1087 7. Schirone, R.C., and Gross, L. (1968). Effect of temperature on early embryological development of
1088 the zebra fish, Brachydanio rerio. J. Exp. Zool. *169*, 43–52. 10.1002/jez.1401690106.
1089 8. Dorrity, M.W., Saunders, L.M., Duran, M., Srivatsan, S.R., Barkan, E., Jackson, D.L., Sattler, S.M.,
1090 Ewing, B., Queitsch, C., Shendure, J., et al. (2023). Proteostasis governs differential temperature
1091 sensitivity across embryonic cell types. Cell *186*, 5015-5027.e12. 10.1016/j.cell.2023.10.013.
1092 9. Lillie, F.R., and Knowlton, F.P. (1897). On the effect of temperature on the development of animals.
1093 Zool. Bull. *1*, 179–193. 10.2307/1535428.
1094 10. Crapse, J., Pappireddi, N., Gupta, M., Shvartsman, S.Y., Wieschaus, E.F., and Wühr, M. (2021).
1095 Evaluating the Arrhenius equation for developmental processes. Mol. Syst. Biol. *17*, e9895.
1096 10.15252/msb.20209895.
1097 11. Kuntz, S.G., and Eisen, M.B. (2014). Drosophila embryogenesis scales uniformly across temperature
1098 in developmentally diverse species. PLoS Genet. *10*, e1004293. 10.1371/journal.pgen.1004293.
1099 12. Chong, J., Amourda, C., and Saunders, T.E. (2018). Temporal development of Drosophila embryos is
1100 highly robust across a wide temperature range. Interface *15*. 10.1098/rsif.2018.0304.
1101 13. Welte, M.A., Tetrault, J.M., Dellavalle, R.P., and Lindquist, S.L. (1993). A new method for
1102 manipulating transgenes: engineering heat tolerance in a complex, multicellular organism. Curr. Biol.
1103 *3*, 842–853. 10.1016/0960-9822(93)90218-D.
1104 14. Foe, V.E., and Alberts, B.M. (1983). Studies of nuclear and cytoplasmic behaviour during the five
1105 mitotic cycles that precede gastrulation in Drosophila embryogenesis. J. Cell Sci. *61*, 31–70.
1106 10.1242/jcs.61.1.31.
1107 15. Xie, Y., and Blankenship, J.T. (2018). Differentially-dimensioned furrow formation by zygotic gene
1108 expression and the MBT. PLoS Genet. *14*, e1007174. 10.1371/journal.pgen.1007174.
1109 16. Mazumdar, A., and Mazumdar, M. (2002). How one becomes many: blastoderm cellularization in
1110 Drosophila melanogaster. BioEssays *24*, 1012–1022. 10.1002/bies.10184.
1111 17. Martin, A.C. (2020). The Physical Mechanisms of Drosophila Gastrulation: Mesoderm and Endoderm
1112 Invagination. Genetics *214*, 543–560. 10.1534/genetics.119.301292.
1113 18. Lecuit, T., and Yap, A.S. (2015). E-cadherin junctions as active mechanical integrators in tissue
1114 dynamics. Nat. Cell Biol. *17*, 533–539. 10.1038/ncb3136.
1115 19. Foe, V.E. (1989). Mitotic domains reveal early commitment of cells in Drosophila embryos. Trends
1116 Genet. *5*, 322. 10.1016/0168-9525(89)90120-0.
1117 20. Niemuth, J., and Wolf, R. (1995). Developmental asynchrony caused by steep temperature gradients
1118 does not impair pattern formation in the wasp, Pimpla turionellae L. Roux's Arch. Dev. Biol. *204*,
1119 444–452. 10.1007/BF00360852.
1120 21. Lucchetta, E.M., Lee, J.H., Fu, L.A., Patel, N.H., and Ismagilov, R.F. (2005). Dynamics of Drosophila
1121 embryonic patterning network perturbed in space and time using microfluidics. Nature *434*, 1134–
1122 1138. 10.1038/nature03509.
1123 22. Kanesaki, T., Edwards, C.M., Schwarz, U.S., and Grosshans, J. (2011). Dynamic ordering of nuclei in
1124 syncytial embryos: a quantitative analysis of the role of cytoskeletal networks. Integr. Biol. (Camb).
1125 *3*, 1112–1119. 10.1039/c1ib00059d.
1126 23. Schmidt, A., and Grosshans, J. (2018). Dynamics of cortical domains in early Drosophila
1127 development. J. Cell Sci. *131*. 10.1242/jcs.212795.
1128 24. Deneke, V.E., Melbinger, A., Vergassola, M., and Di Talia, S. (2016). Waves of Cdk1 Activity in S Phase
1129 Synchronize the Cell Cycle in Drosophila Embryos. Dev. Cell *38*, 399–412.
1130 10.1016/j.devcel.2016.07.023.
1131 25. Harris, T.J.C., and Peifer, M. (2004). Adherens junction-dependent and -independent steps in the
1132 establishment of epithelial cell polarity in Drosophila. J. Cell Biol. *167*, 135–147.
1133 10.1083/jcb.200406024.

1134 26. Cao, J., Crest, J., Fasulo, B., and Sullivan, W. (2010). Cortical actin dynamics facilitate early-stage
1135 centrosome separation. Curr. Biol. *20*, 770–776. 10.1016/j.cub.2010.02.060.
1136 27. Rizzelli, F., Malabarba, M.G., Sigismund, S., and Mapelli, M. (2020). The crosstalk between
1137 microtubules, actin and membranes shapes cell division. Open Biol. *10*, 190314.
1138 10.1098/rsob.190314.
1139 28. McCartney, B.M., McEwen, D.G., Grevengoed, E., Maddox, P., Bejsovec, A., and Peifer, M. (2001).
1140 Drosophila APC2 and Armadillo participate in tethering mitotic spindles to cortical actin. Nat. Cell
1141 Biol. *3*, 933–938. 10.1038/ncb1001-933.
1142 29. Rim, E.Y., Clevers, H., and Nusse, R. (2022). The Wnt Pathway: From Signaling Mechanisms to
1143 Synthetic Modulators. Annu. Rev. Biochem. *91*, 571–598. 10.1146/annurev-biochem-040320-
1144 103615.
1145 30. Mapelli, M., and Gonzalez, C. (2012). On the inscrutable role of Inscuteable: structural basis and
1146 functional implications for the competitive binding of NuMA and Inscuteable to LGN. Open Biol. *2*,
1147 120102. 10.1098/rsob.120102.
1148 31. Lynch, J.A., El-Sherif, E., and Brown, S.J. (2012). Comparisons of the embryonic development of
1149 Drosophila , Nasonia , and Tribolium. Wiley Interdiscip. Rev. Dev. Biol. *1*, 16–39. 10.1002/wdev.3.
1150 32. Lemke, S., Kale, G., and Urbansky, S. (2020). Comparing gastrulation in flies: Links between cell
1151 biology and the evolution of embryonic morphogenesis. Mech. Dev. *164*, 103648.
1152 10.1016/j.mod.2020.103648.
1153 33. Cadigan, K.M., and Nusse, R. (1997). Wnt signaling: a common theme in animal development. Genes
1154 Dev. *11*, 3286–3305. 10.1101/gad.11.24.3286.
1155 34. Pires-daSilva, A., and Sommer, R.J. (2003). The evolution of signalling pathways in animal
1156 development. Nat. Rev. Genet. *4*, 39–49. 10.1038/nrg977.
1157 35. Long, Y.C., Chin Tan, T.M., Takao, I., and Tang, B.L. (2014). The biochemistry and cell biology of
1158 aging: Metabolic regulation through mitochondrial signaling. Am. J. Physiol. - Endocrinol. Metab.
1159 *306*. 10.1152/ajpendo.00665.2013.
1160 36. Bitto, A., Wang, A.M., Bennett, C.F., and Kaeberlein, M. (2015). Biochemical genetic pathways that
1161 modulate aging in multiple species. Cold Spring Harb. Perspect. Med. *5*, 1–25.
1162 10.1101/cshperspect.a025114.
1163 37. Hale, R., and Strutt, D. (2015). Conservation of Planar Polarity Pathway Function Across the Animal
1164 Kingdom. Annu. Rev. Genet. *49*, 529–551. 10.1146/annurev-genet-112414-055224.
1165 38. Wright, B.A., Kvansakul, M., Schierwater, B., and Humbert, P.O. (2022). Cell polarity signalling at the
1166 birth of multicellularity: What can we learn from the first animals. Front. Cell Dev. Biol. *10*, 1–19.
1167 10.3389/fcell.2022.1024489.
1168 39. Schlacht, A., Herman, E.K., Klute, M.J., Field, M.C., and Dacks, J.B. (2014). Missing Pieces of an
1169 Ancient Puzzle: Evolution of the Eukaryotic Membrane-Trafficking System. Cold Spring Harb.
1170 Perspect. Biol. *6*, a016048–a016048. 10.1101/cshperspect.a016048.
1171 40. Harashima, H., Dissmeyer, N., and Schnittger, A. (2013). Cell cycle control across the eukaryotic
1172 kingdom. Trends Cell Biol. *23*, 345–356. 10.1016/j.tcb.2013.03.002.
1173 41. Erickson, H.P. (2007). Evolution of the cytoskeleton. BioEssays *29*, 668–677. 10.1002/bies.20601.
1174 42. Wickstead, B., and Gull, K. (2011). The evolution of the cytoskeleton. J. Cell Biol. *194*, 513–525.
1175 10.1083/jcb.201102065.
1176 43. Vazquez, J., Pauli, D., and Tissières, A. (1993). Transcriptional regulation in Drosophila during heat
1177 shock: a nuclear run-on analysis. Chromosoma *102*, 233–248. 10.1007/BF00352397.
1178 44. Leemans, R., Egger, B., Loop, T., Kammermeier, L., He, H., Hartmann, B., Certa, U., Hirth, F., and
1179 Reichert, H. (2000). Quantitative transcript imaging in normal and heat-shocked Drosophila embryos
1180 by using high-density oligonucleotide arrays. Proc. Natl. Acad. Sci. *97*, 12138–12143.
1181 10.1073/pnas.210066997.

1182 45. Feder, M.E., Cartaño, N. V., Milos, L., Krebs, R.A., and Lindquist, S.L. (1996). Effect of engineering
1183 Hsp70 copy number on Hsp70 expression and tolerance of ecologically relevant heat shock in larvae
1184 and pupae of Drosophila melanogaster. J. Exp. Biol. *199*, 1837–1844. 10.1242/jeb.199.8.1837.

1185 46. Feder, M.E., Blair, N., and Figueras, H. (1997). Natural thermal stress and heat-shock protein
1186 expression in Drosophila larvae and pupae. Funct. Ecol. *11*, 90–100. 10.1046/j.1365-
1187 2435.1997.00060.x.

1188 47. Sørensen, J.G., Nielsen, M.M., Kruhøffer, M., Justesen, J., and Loeschcke, V. (2005). Full genome
1189 gene expression analysis of the heat stress response in Drosophila melanogaster. Cell Stress
1190 Chaperones *10*, 312–328. 10.1379/csc-128r1.1.

1191 48. Lockwood, B.L., Julick, C.R., and Montooth, K.L. (2017). Maternal loading of a small heat shock
1192 protein increases embryo thermal tolerance in Drosophila melanogaster. J. Exp. Biol. *220*, 4492–
1193 4501. 10.1242/jeb.164848.

1194 49. Rutherford, S.L., and Lindquist, S. (1998). Hsp90 as a capacitor for morphological evolution. Nature
1195 *396*, 336–342. 10.1038/24550.

1196 50. Sangster, T.A., Lindquist, S., and Queitsch, C. (2004). Under cover: causes, effects and implications of
1197 Hsp90-mediated genetic capacitance. BioEssays *26*, 348–362. 10.1002/bies.20020.

1198 51. IPBES (2019). The global assessment report of the Intergovernmental Science-Policy Platform on
1199 Biodiversity and Ecosystem Services.

1200 52. Raguso, R.A. (2020). Don't forget the flies: dipteran diversity and its consequences for floral ecology
1201 and evolution. Appl. Entomol. Zool. *55*, 1–7. 10.1007/s13355-020-00668-9.

1202 53. Bogovic, J.A., Hanslovsky, P., Wong, A., and Saalfeld, S. (2016). Robust registration of calcium images
1203 by learned contrast synthesis. In 2016 IEEE 13th International Symposium on Biomedical Imaging
1204 (ISBI) (IEEE), pp. 1123–1126. 10.1109/ISBI.2016.7493463.

1205 54. Pietzsch, T., Saalfeld, S., Preibisch, S., and Tomancak, P. (2015). BigDataViewer: visualization and
1206 processing for large image data sets. Nat. Methods *12*, 481–483. 10.1038/nmeth.3392.

1207 55. Preibisch, S., Saalfeld, S., and Tomancak, P. (2009). Globally optimal stitching of tiled 3D microscopic
1208 image acquisitions. Bioinformatics *25*, 1463–1465. 10.1093/bioinformatics/btp184.

1209 56. Ollion, J., Cochennec, J., Loll, F., Escudé, C., and Boudier, T. (2013). TANGO: a generic tool for high-
1210 throughput 3D image analysis for studying nuclear organization. Bioinformatics *29*, 1840–1841.
1211 10.1093/bioinformatics/btt276.

1212 57. Herbert, S., Valon, L., Mancini, L., Dray, N., Caldarelli, P., Gros, J., Esposito, E., Shorte, S.L., Bally-Cuif,
1213 L., Aulner, N., et al. (2021). LocalZProjector and DeProj: a toolbox for local 2D projection and
1214 accurate morphometrics of large 3D microscopy images. BMC Biol. *19*, 136. 10.1186/s12915-021-
1215 01037-w.

1216 58. Edgar, B.A., Kiehle, C.P., and Schubiger, G. (1986). Cell cycle control by the nucleo-cytoplasmic ratio
1217 in early Drosophila development. Cell *44*, 365–372. 10.1016/0092-8674(86)90771-3.

1218 59. Lu, X., Li, J.M., Elemento, O., Tavazoie, S., and Wieschaus, E.F. (2009). Coupling of zygotic
1219 transcription to mitotic control at the Drosophila mid-blastula transition. Development *136*, 2101–
1220 2110. 10.1242/dev.034421.

1221 60. Telley, I.A., Gáspár, I., Ephrussi, A., and Surrey, T. (2012). Aster migration determines the length
1222 scale of nuclear separation in the Drosophila syncytial embryo. J. Cell Biol. *197*, 887–895.
1223 10.1083/jcb.201204019.

1224 61. Oakeshott, J.G., McKechnie, S.W., and Chambers, G.K. (1984). Population genetics of the
1225 metabolically related Adh, Gpdh and Tpi polymorphisms in Drosophila melanogaster I. Geographic
1226 variation in Gpdh and Tpi allele frequencies in different continents. Genetica *63*, 21–29.
1227 10.1007/BF00137461.

1228 62. McColl, G., and McKechnie, S.W. (1999). The Drosophila heat shock hsr-omega gene: An allele
1229 frequency cline detected by quantitative PCR. Mol. Biol. Evol. *16*, 1568–1574.
1230 10.1093/oxfordjournals.molbev.a026069.

1231 63. Bettencourt, B.R., Kim, I., Hoffmann, A.A., and Feder, M.E. (2002). Response to natural and
1232 laboratory selection at the Drosophila hsp70 genes. Evolution (N. Y). *56*, 1796–1801.
1233 10.1111/j.0014-3820.2002.tb00193.x.

1234 64. Frydenberg, J., Hoffmann, A.A., and Loeschcke, V. (2003). DNA sequence variation and latitudinal
1235 associations in hsp23, hsp26 and hsp27 from natural populations of Drosophila melanogaster. Mol.
1236 Ecol. *12*, 2025–2032. 10.1046/j.1365-294X.2002.01882.x.

1237 65. Umina, P.A., Weeks, A.R., Kearney, M.R., McKechnie, S.W., and Hoffmann, A.A. (2005). Evolution: A
1238 rapid shift in a classic clinal pattern in Drosophila reflecting climate change. Science (80-.). *308*,
1239 691–693. 10.1126/science.1109523.

1240 66. Sawyer, L.A., Sandrelli, F., Pasetto, C., Peixoto, A.A., Rosato, E., Costa, R., and Kyriacou, C.P. (2006).
1241 The period gene Thr-Gly polymorphism in Australian and African Drosophila melanogaster
1242 populations: Implications for selection. Genetics *174*, 465–480. 10.1534/genetics.106.058792.

1243 67. Weeks, A.R., Mckechnie, S.W., and Hoffmann, A.A. (2006). In search of clinal variation in the period
1244 and clock timing genes in Australian Drosophila melanogaster populations. J. Evol. Biol. *19*, 551–557.
1245 10.1111/j.1420-9101.2005.01013.x.

1246 68. Rand, D.M., Weinreich, D.M., Lerman, D., Folk, D., and Gilchrist, G.W. (2010). Three selections are
1247 better than one: Clinal variation of thermal QTL from independent selection experiments in
1248 drosophila. Evolution (N. Y). *64*, 2921–2934. 10.1111/j.1558-5646.2010.01039.x.

1249 69. Kolaczkowski, B., Kern, A.D., Holloway, A.K., and Begun, D.J. (2011). Genomic differentiation
1250 between temperate and tropical Australian populations of Drosophila melanogaster. Genetics *187*,
1251 245–260. 10.1534/genetics.110.123059.

1252 70. Paaby, A.B., Bergland, A.O., Behrman, E.L., and Schmidt, P.S. (2014). A highly pleiotropic amino acid
1253 polymorphism in the Drosophila insulin receptor contributes to life-history adaptation. Evolution *68*,
1254 3395–3409. 10.1111/evo.12546.

1255 71. Vigue, C.L., and Johnson, F.M. (1973). Isozyme Variability in Species of the Genus Drosophila. VI.
1256 Frequency-Property-Environment Relationships of Allelic Alcohol Dehydrogenases in D.
1257 melanogaster. Biochem. Genet. *9*, 213–227.

1258 72. Berry, A., and Kreitman, M. (1993). Molecular analysis of an allozyme cline: alcohol dehydrogenase
1259 in Drosophila melanogaster on the east coast of North America. Genetics *134*, 869–893.
1260 10.1093/genetics/134.3.869.

1261 73. Duvernell, D.D., and Eanes, W.F. (2000). Contrasting molecular population genetics of four
1262 hexokinases in Drosophila melanogaster, D. simulans and D. yakuba. Genetics *156*, 1191–1201.
1263 10.1093/genetics/156.3.1191.

1264 74. Schmidt, P.S., Duvernell, D.D., and Eanes, W.F. (2000). Adaptive evolution of a candidate gene for
1265 aging in Drosophila. Proc. Natl. Acad. Sci. *97*, 10861–10865. 10.1073/pnas.190338897.

1266 75. Verrelli, B.C., and Eanes, W.F. (2001). Clinal variation for amino acid polymorphisms at the Pgm locus
1267 in Drosophila melanogaster. Genetics *157*, 1649–1663. 10.1093/genetics/157.4.1649.

1268 76. Duvernell, D.D., Schmidt, P.S., and Eanes, W.F. (2003). Clines and adaptive evolution in the
1269 methuselah gene region in Drosophila melanogaster. Mol. Ecol. *12*, 1277–1285. 10.1046/j.1365-
1270 294X.2003.01841.x.

1271 77. Sezgin, E., Duvernell, D.D., Matzkin, L.M., Duan, Y., Zhu, C.T., Verrelli, B.C., and Eanes, W.F. (2004).
1272 Single-locus latitudinal clines and their relationship to temperate adaptation in metabolic genes and
1273 derived alleles in Drosophila melanogaster. Genetics *168*, 923–931. 10.1534/genetics.104.027649.

1274 78. Schmidt, P.S., and Paaby, A.B. (2008). Reproductive diapause and life-history clines in North
1275 American populations of Drosophila melanogaster. Evolution (N. Y). *62*, 1204–1215. 10.1111/j.1558-
1276 5646.2008.00351.x.

1277 79. Fabian, D.K., Kapun, M., Nolte, V., Kofler, R., Schmidt, P.S., Schlötterer, C., and Flatt, T. (2012).
1278 Genome-wide patterns of latitudinal differentiation among populations of Drosophila melanogaster
1279 from North America. Mol. Ecol. *21*, 4748–4769. 10.1111/j.1365-294X.2012.05731.x.

80. Machado, H.E., Bergland, A.O., O'Brien, K.R., Behrman, E.L., Schmidt, P.S., and Petrov, D.A. (2016). Comparative population genomics of latitudinal variation in Drosophila simulans and Drosophila melanogaster. Mol. Ecol. *25*, 723–740. 10.1111/mec.13446.

81. Costa, R., Peixoto, A.A., Barbujani, G., and Kyriacou, C.P. (1992). A latitudinal cline in a Drosophila clock gene. Proc. R. Soc. London, 43–49.

82. Kapun, M., Barrón, M.G., Staubach, F., Obbard, D.J., Wiberg, R.A.W., Vieira, J., Goubert, C., Rota-Stabelli, O., Kankare, M., Bogaerts-Márquez, M., et al. (2020). Genomic Analysis of European Drosophila melanogaster Populations Reveals Longitudinal Structure, Continent-Wide Selection, and Previously Unknown DNA Viruses. Mol. Biol. Evol. *37*, 2661–2678. 10.1093/molbev/msaa120.

83. Graveley, B.R., Brooks, A.N., Carlson, J.W., Duff, M.O., Landolin, J.M., Yang, L., Artieri, C.G., van Baren, M.J., Boley, N., Booth, B.W., et al. (2011). The developmental transcriptome of Drosophila melanogaster. Nature *471*, 473–479. 10.1038/nature09715.

Figure 1

Increased embryonic lethality at elevated temperature

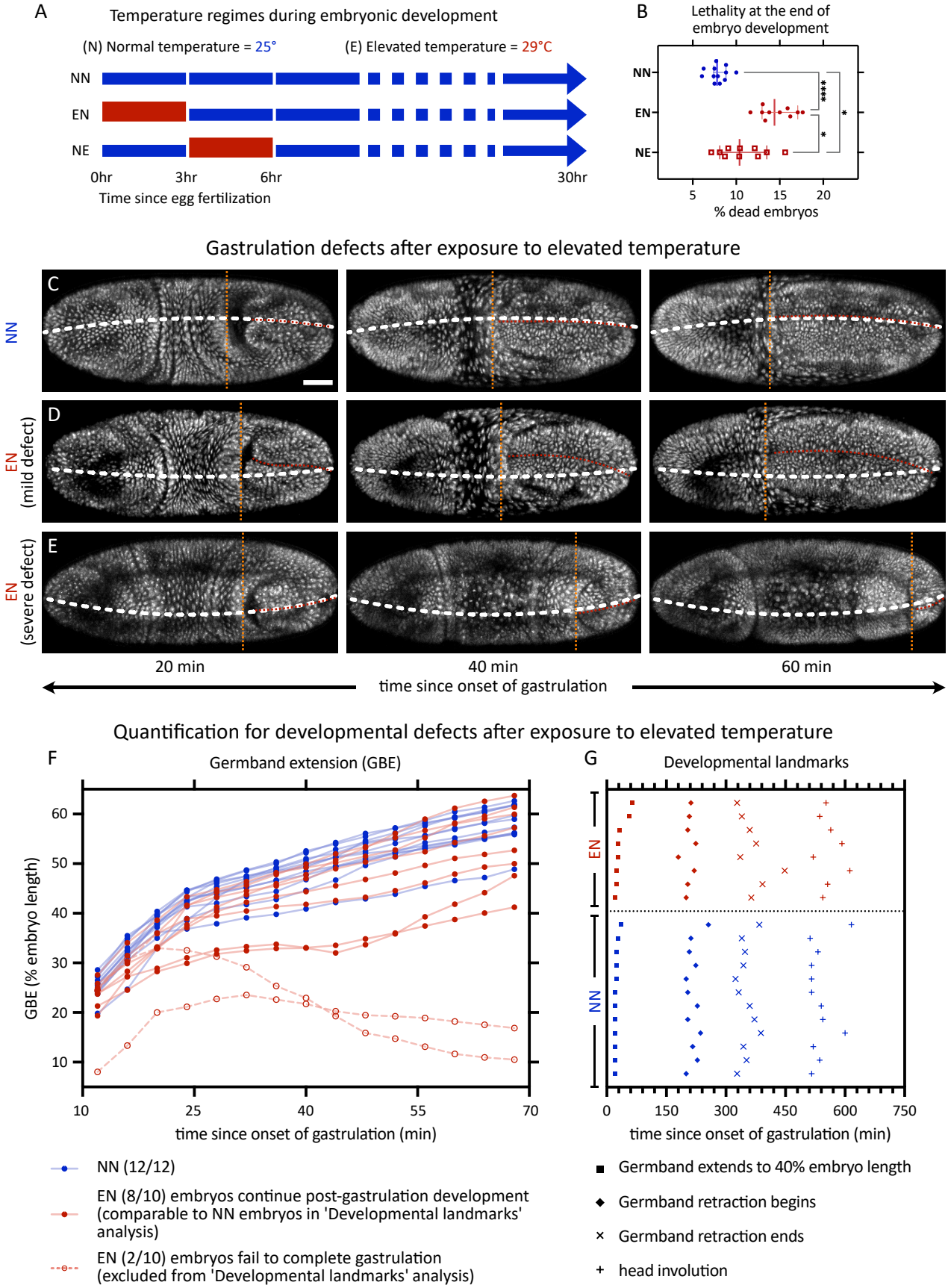

Figure 2

Bilaterally asymmetric loss of nuclei and blastoderm holes

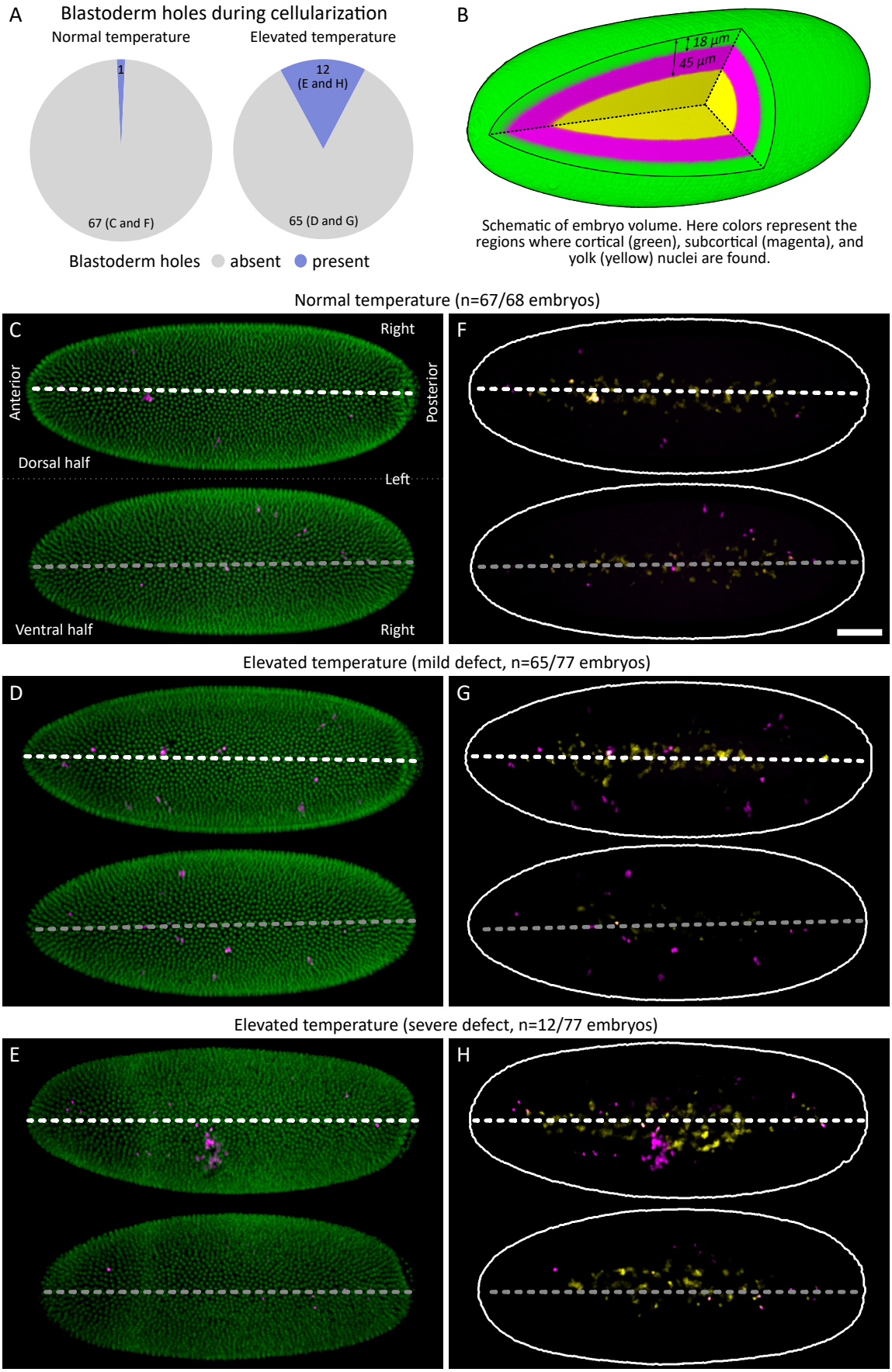

Figure 3

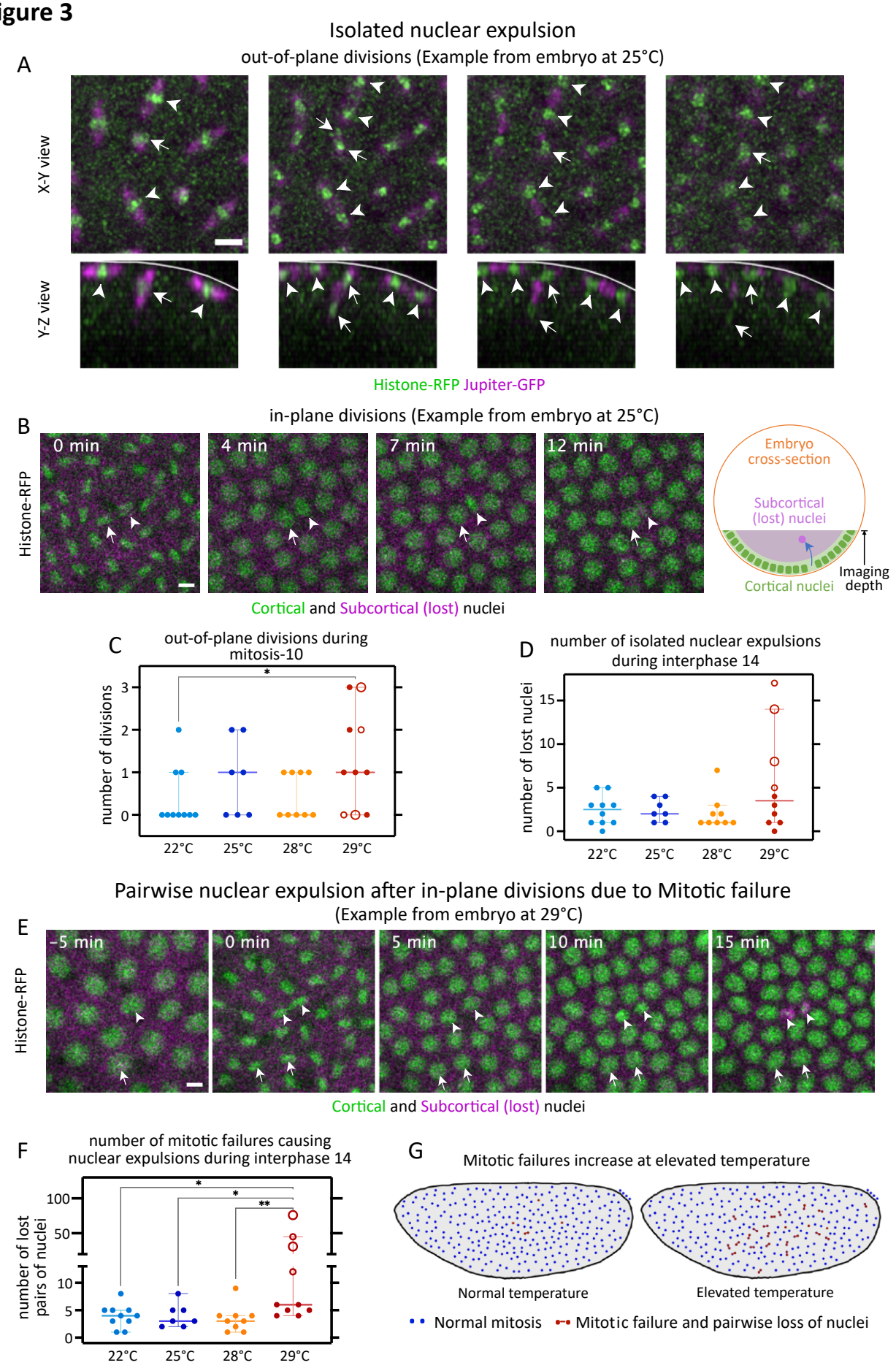
Isolated nuclear expulsion
A
out-of-plane divisions (Example from embryo at 25°C)
X-Y view
Y-Z view
Histone-RFP Jupiter-GFP
B
in-plane divisions (Example from embryo at 25°C)
Histone-RFP
0 min
4 min
7 min
12 min
Embryo cross-section
Subcortical (lost) nuclei
Cortical nuclei
Imaging depth
Cortical and Subcortical (lost) nuclei
C
out-of-plane divisions during mitosis-10
number of divisions
22°C
25°C
28°C
29°C
D
number of isolated nuclear expulsions during interphase 14
number of lost nuclei
Pairwise nuclear expulsion after in-plane divisions due to Mitotic failure
(Example from embryo at 29°C)
E
Histone-RFP
-5 min
0 min
5 min
10 min
15 min
Cortical and Subcortical (lost) nuclei
F
number of mitotic failures causing nuclear expulsions during interphase 14
number of lost pairs of nuclei
G
Mitotic failures increase at elevated temperature
Normal temperature
Elevated temperature
Normal mitosis
Mitotic failure and pairwise loss of nuclei

Figure 4

Asynchrony in the phases of nuclear division cycles at elevated temperature

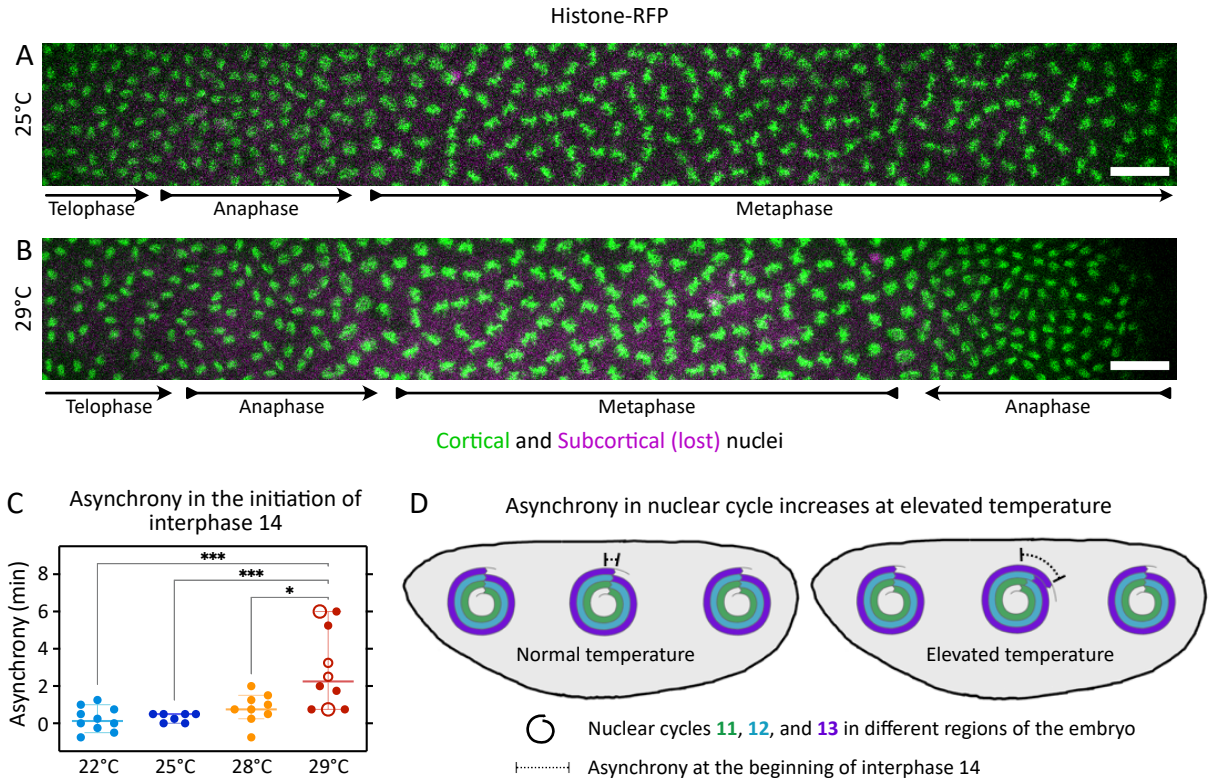

Figure 5

Increased nuclear crowding at elevated temperature

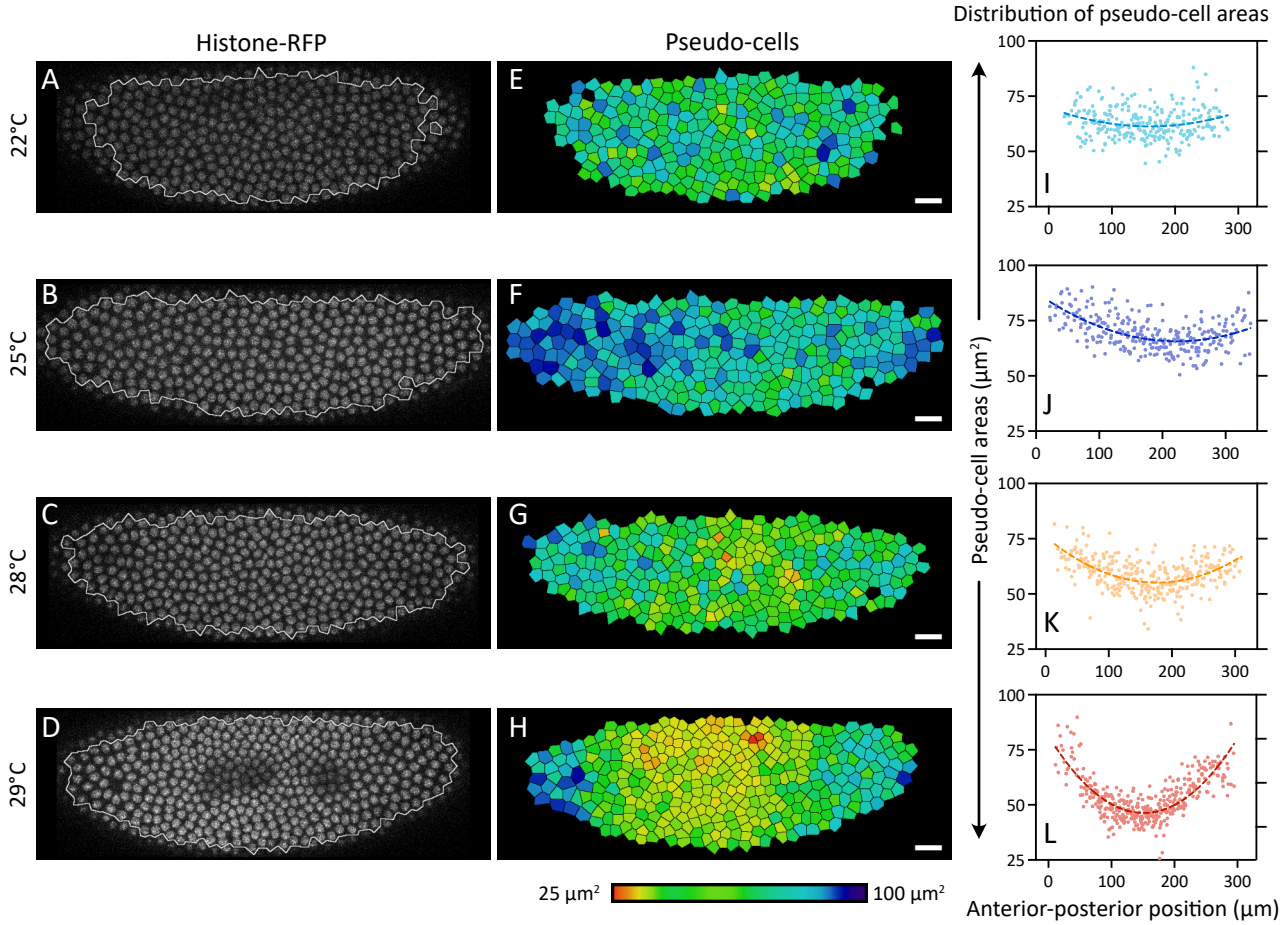

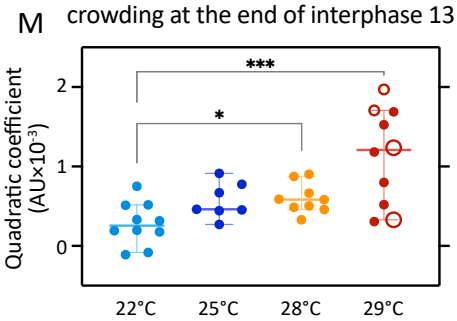

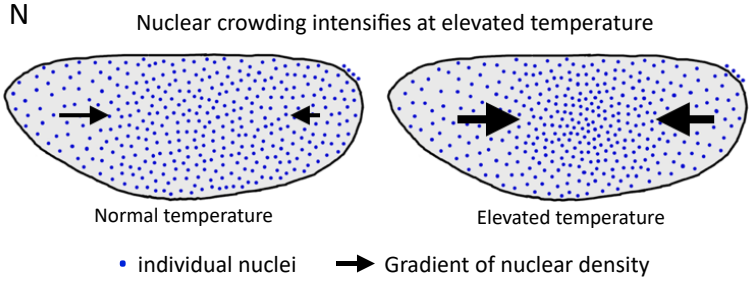

Figure 6 combinatorial effects of nuclear crowding and nuclear cycle asynchrony on distribution of mitotic failures at elevated temperature

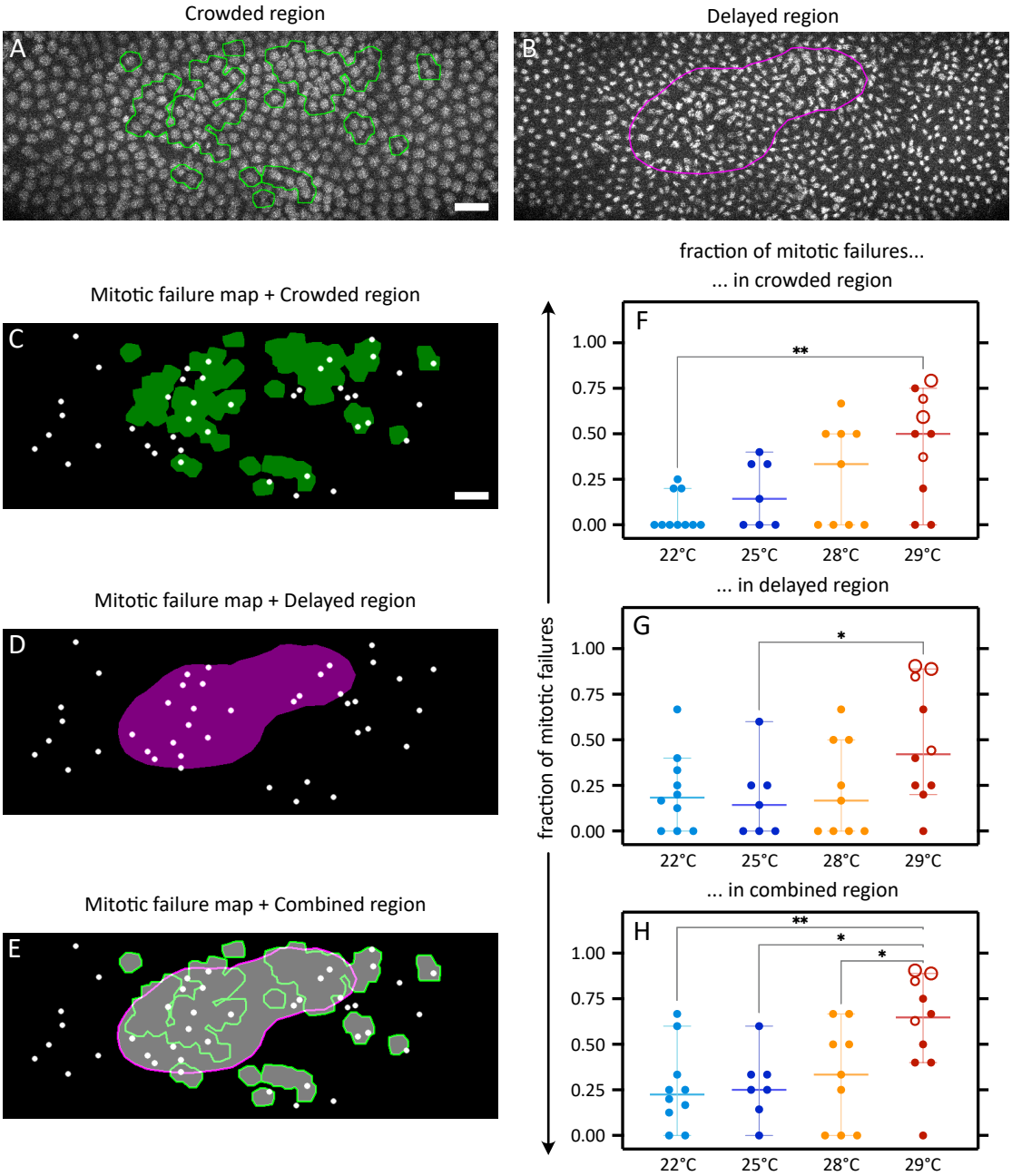

Figure 7

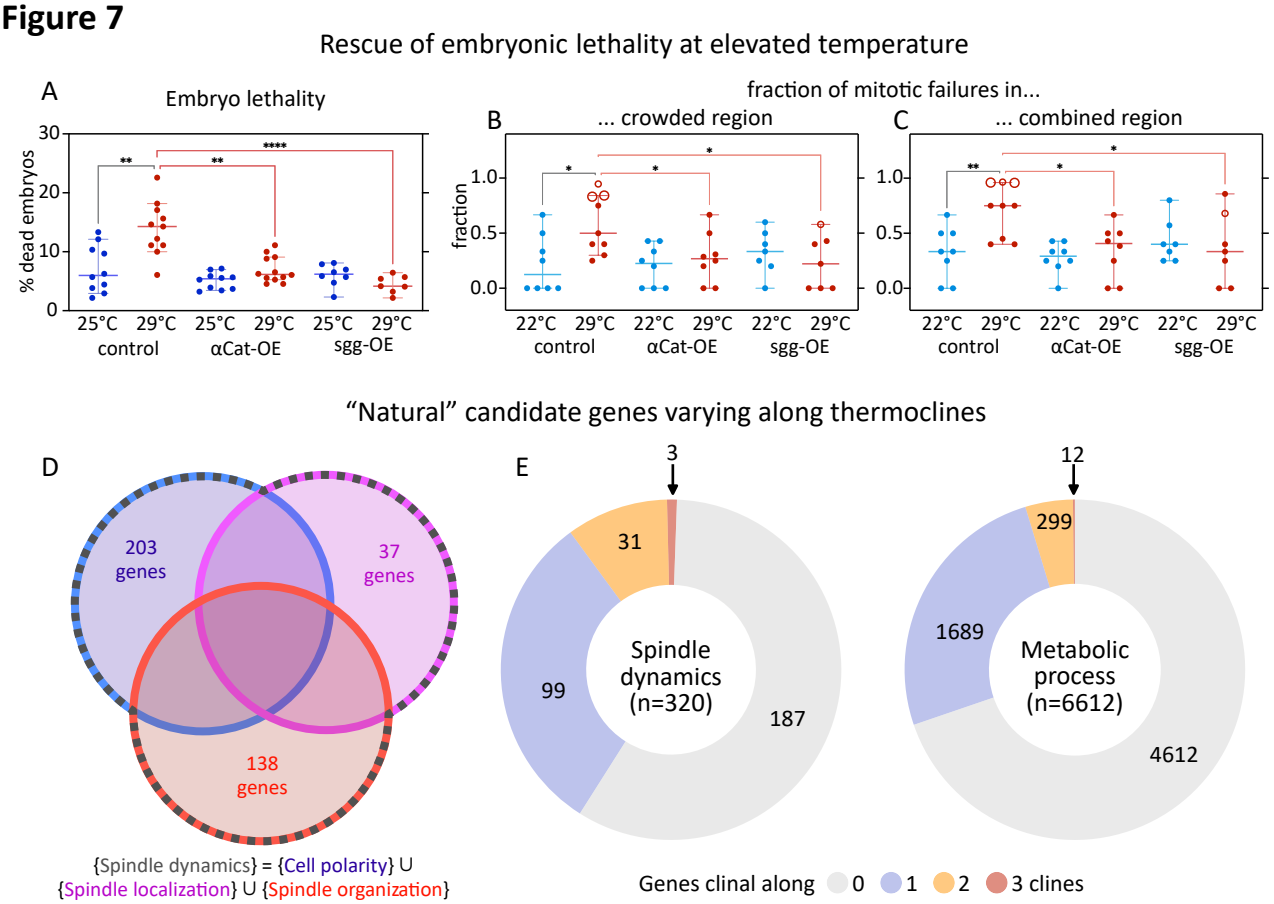
Rescue of embryonic lethality at elevated temperature
A
Embryo lethality
% dead embryos
30
20
10
0
**
**
****
25°C 29°C 25°C 29°C 25°C 29°C
control αCat-OE sgg-OE
fraction of mitotic failures in...
B
... crowded region
C
... combined region
fraction
1.0
0.5
0.0
*
*
*
**
*
*
22°C 29°C 22°C 29°C 22°C 29°C
control αCat-OE sgg-OE
"Natural" candidate genes varying along thermoclines
D
203 genes
37 genes
138 genes
{Spindle dynamics} = {Cell polarity} ∪
{Spindle localization} ∪ {Spindle organization}
E
3
31
99
187
Spindle dynamics (n=320)
12
299
1689
4612
Metabolic process (n=6612)
Genes clinal along 0 1 2 3 clines

Figure S1

Nuclear expulsion at elevated temperature

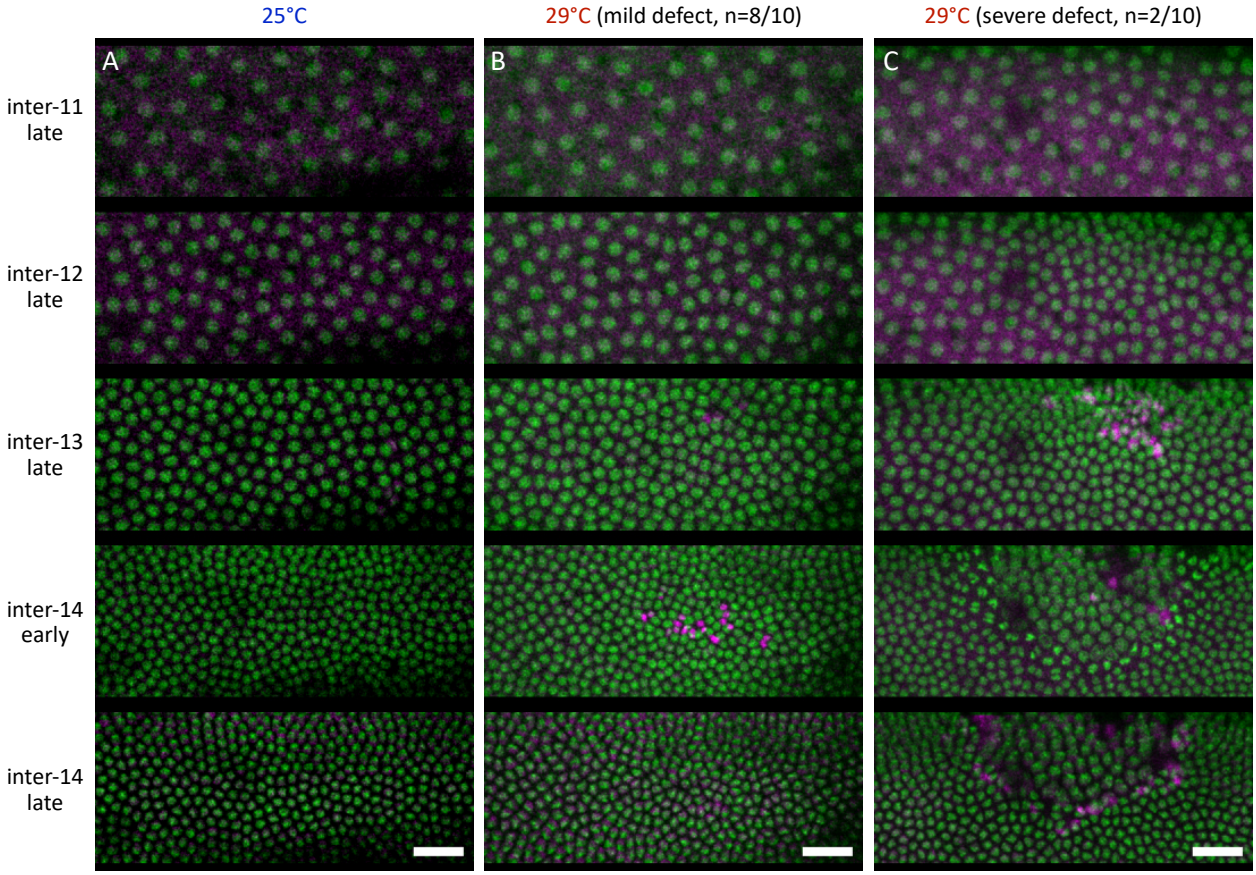

Figure S2

Blastoderm holes at elevated temperature

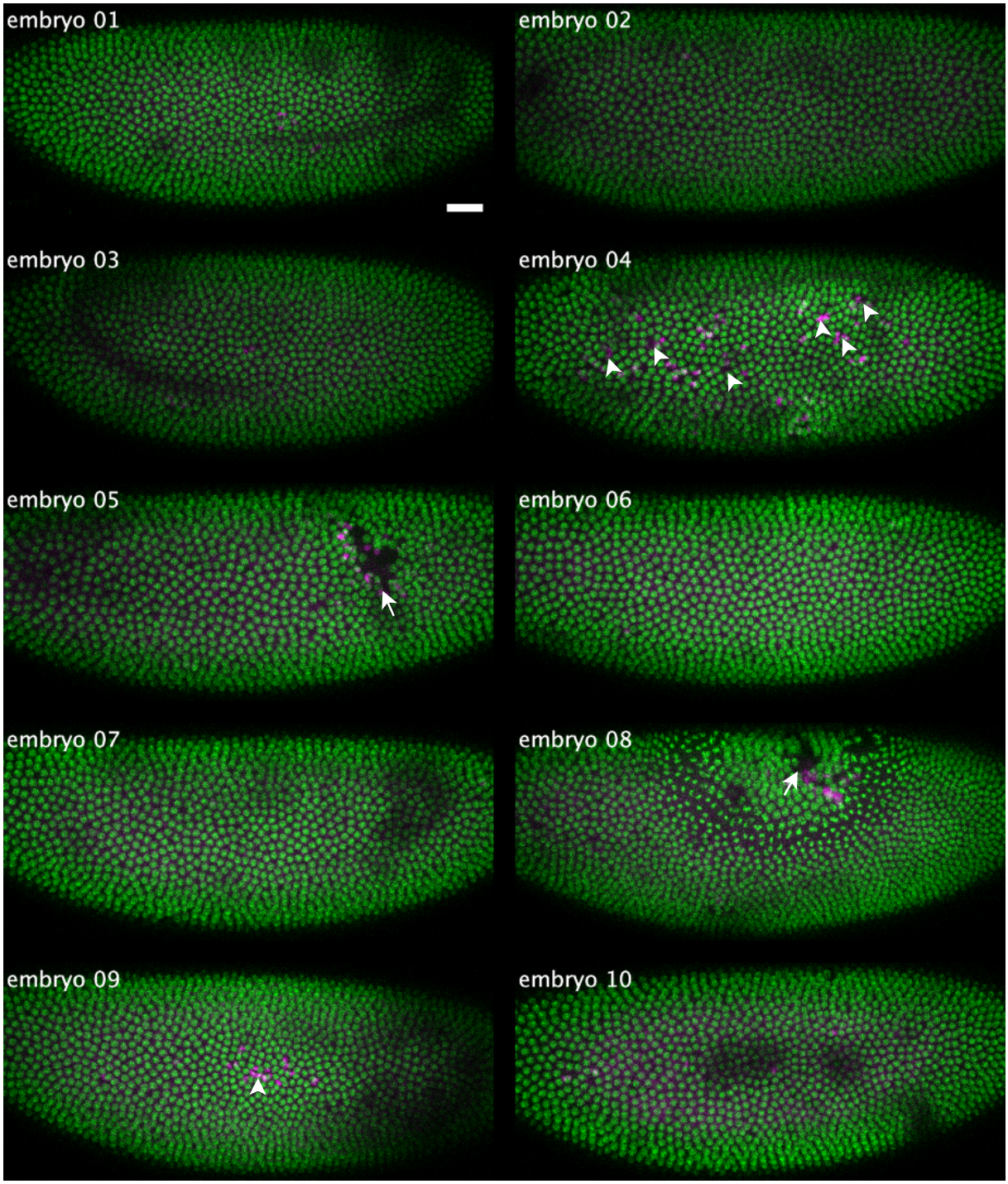

Figure S3

Nuclear expulsion is a passive process

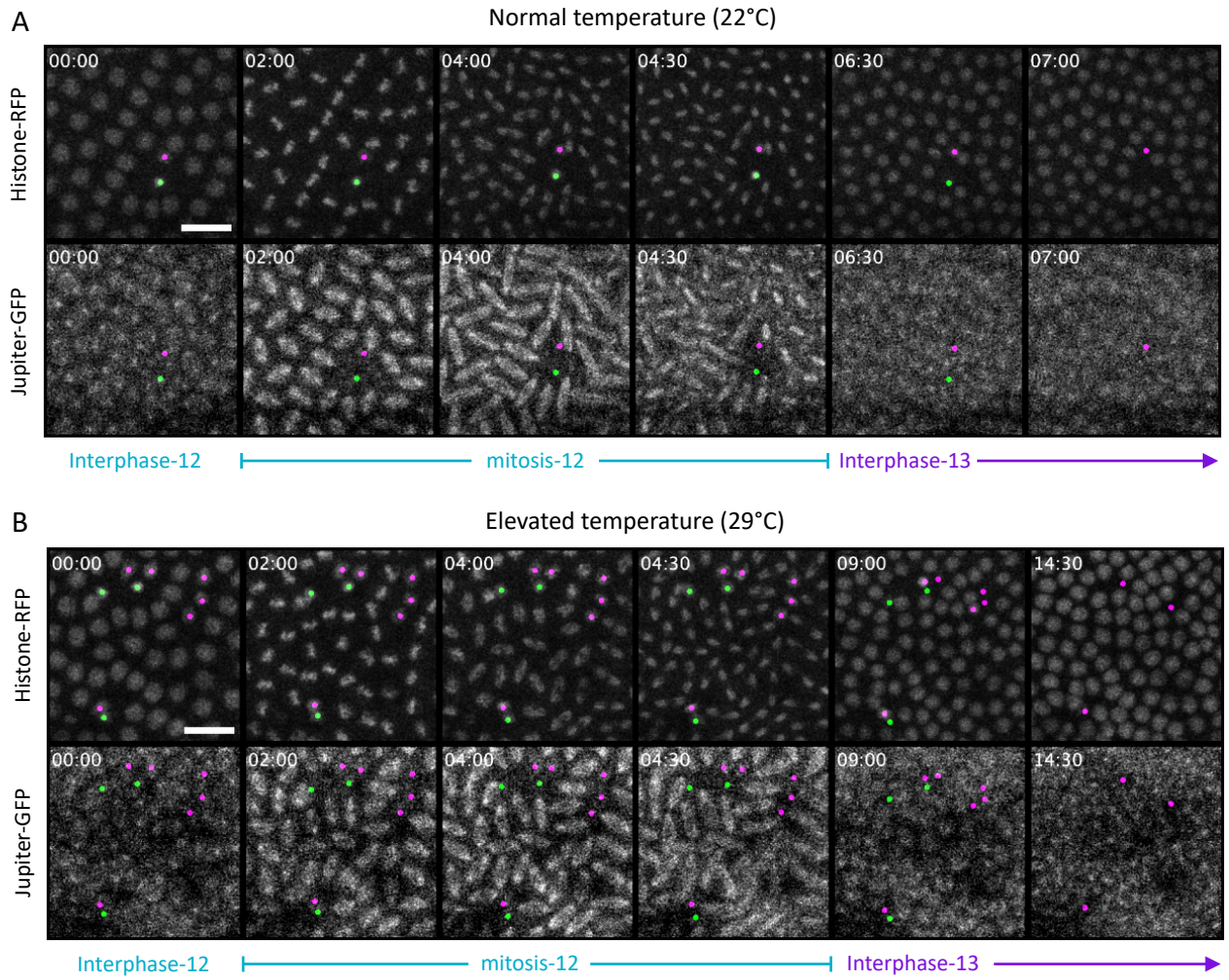

Figure S4

Nuclear cluster drift and deviations in x-y plane

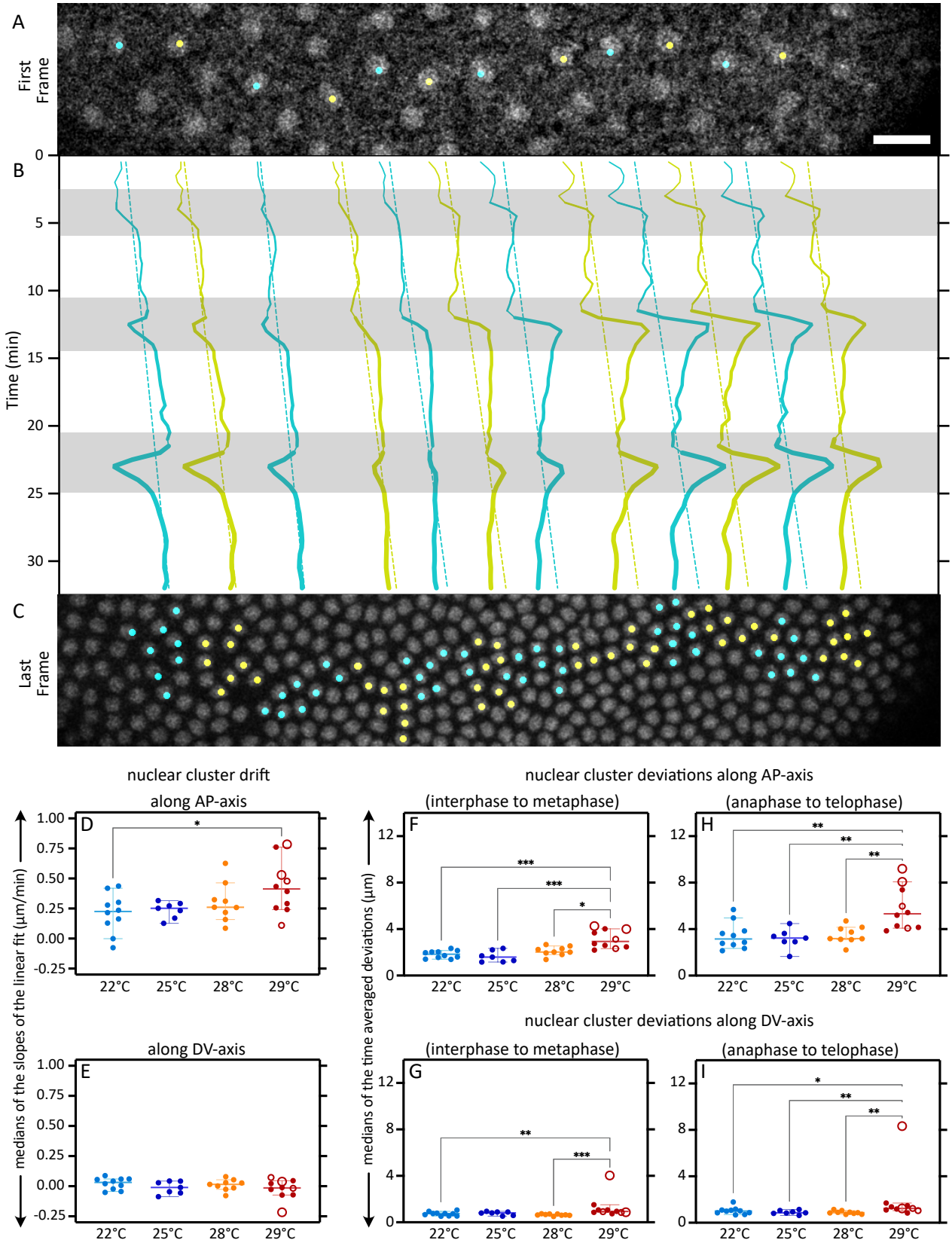

Figure S5

Nuclear movement along z axis at elevated temperature

A Normal temperature (22°C)

B Elevated temperature (29°C)

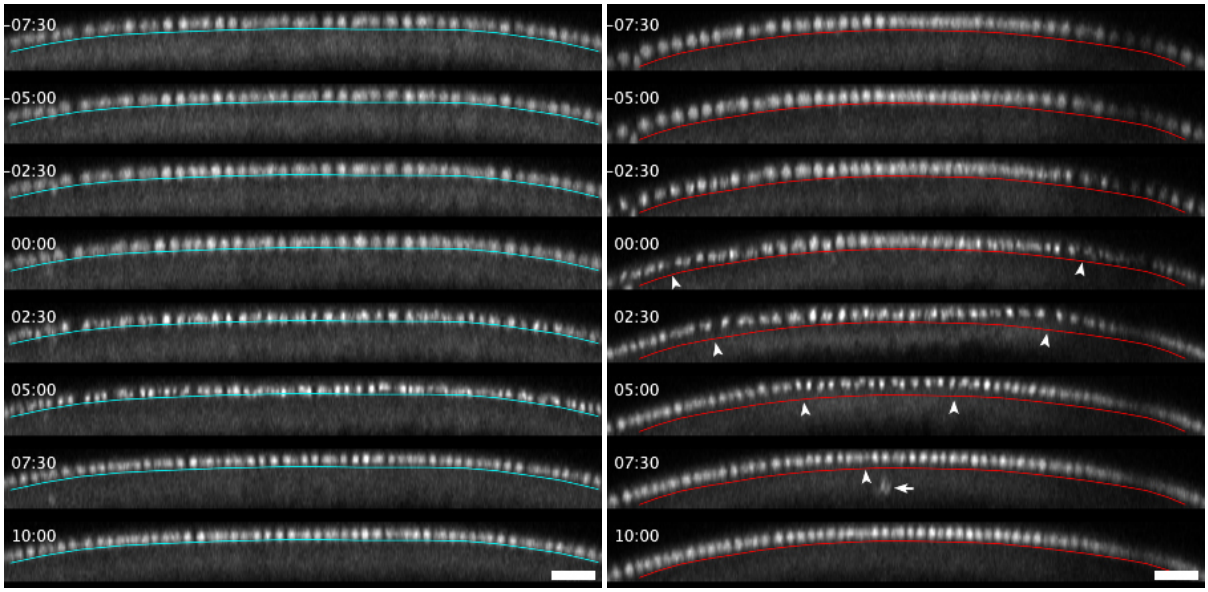

Figure S6

Asynchrony in the phases of nuclear division cycles at elevated temperature

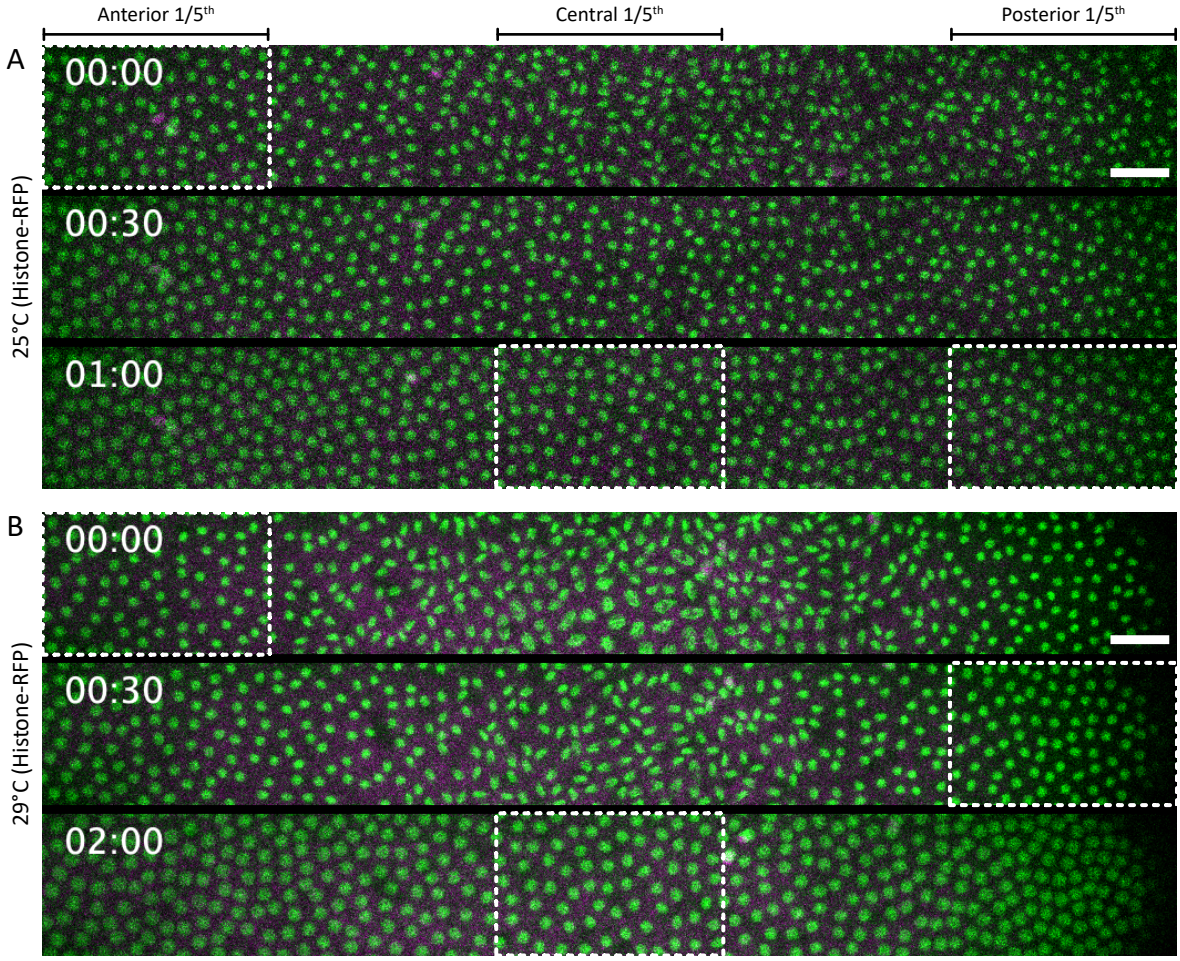

Cortical and Subcortical (lost) nuclei

Figure S7

trends in fraction of mitotic failures can't be explained through trends in area fractions

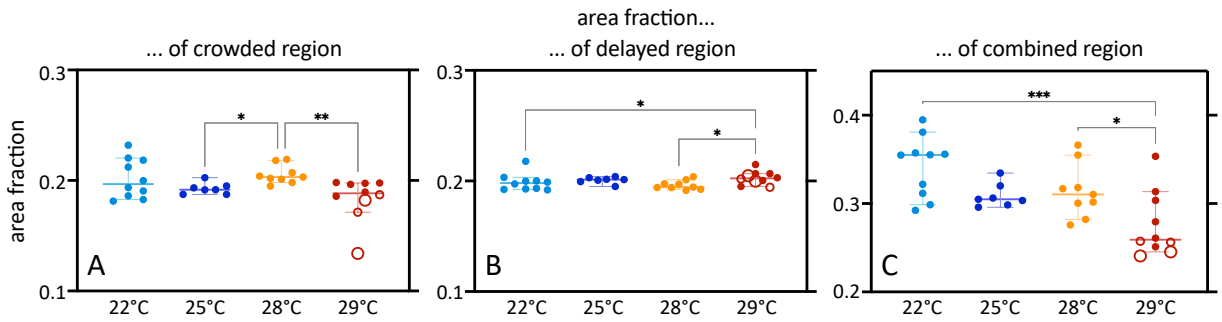

Figure S8

Rescue of embryonic lethality at elevated temperature

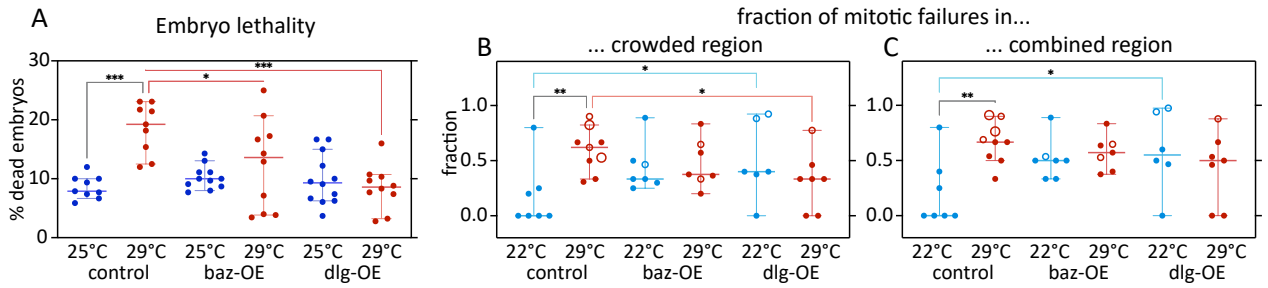

Figure S9

Empty F-actin caps at elevated temperature

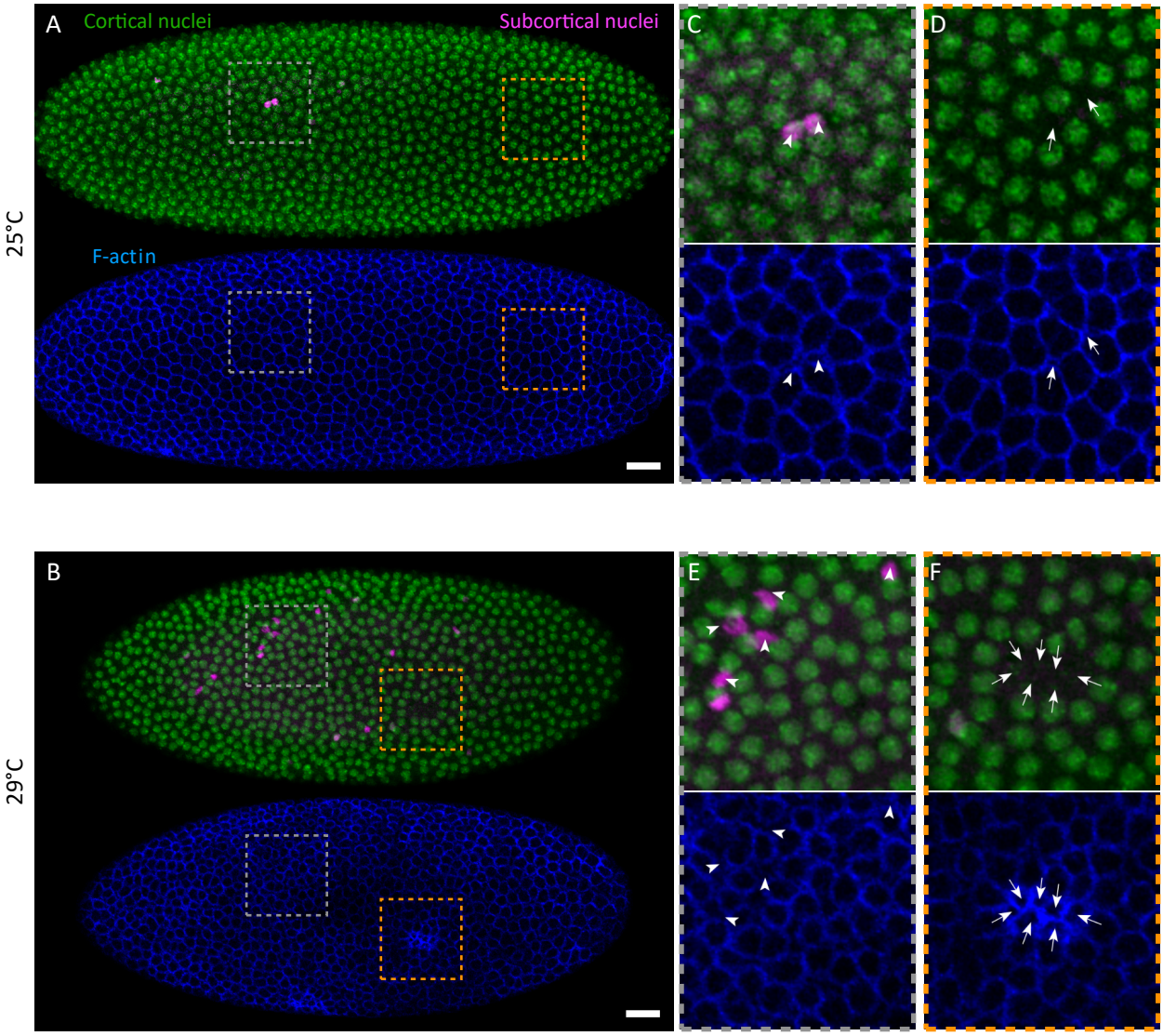

Figure S10
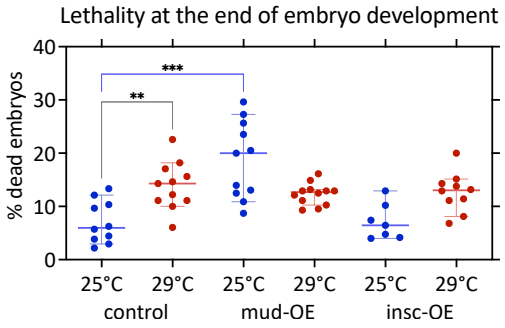
Rescue of embryonic lethality at elevated temperature